Mapping intragranular microstructures in quartz: the significance of Dauphiné twinning

Geoffrey E. Lloyd

Institute of Geophysics and Tectonics, School of Earth and Environment, The Univeriksity of Leeds, Leeds LS2 9JT, UK

0000-0002-7859-2486

Correspondence: G.E.lloyd@leeds.ac.uk

Abstract: Mapping on the microstructural scale can contribute significantly to conventional field and larger scale mapping and understanding of spatial, temporal and process-oriented relationships. Here, electron backscattered diffraction (EBSD)-based microstructural maps are presented of subgrain and Dauphiné twin boundaries in undeformed sedimentary quartzite. 'Plane matching' analysis permits determination of the complete orientation of boundaries. A workflow is presented to facilitate the necessary crystallographic calculations. The resulting maps indicate: (1) boundary plane rotation angle/axis pairs, including tilt–twist components; (2) boundary migration vectors; and (3) conventional EBSD misorientation angle/axis pairs. Subgrain boundaries are general with small misorientations and boundary plane normal directions sub-parallel to grain boundary stress concentrations; rotation axes are oriented sub-parallel to the bedding dip (017°/10°E). Most exhibit bi-direction boundary migration vectors parallel to bedding normal. The EBSD misorientation analysis results are different as they only recognize the parallelism of adjacent crystal lattices. The differences are especially apparent for Dauphiné twin boundaries. Maps are presented of twin boundaries using matched plane analysis, including explanation for lateral twin migration. Driving forces to move twin boundaries are also estimated by mapping variations in Young's modulus between parents and twins; differences are significant, indicating that the Young's modulus and driving forces do not need to be large, explaining the propensity for twinning in many quartzites.

Supplementary material: Graphical solutions for all boundaries, solutions to matched plane and EBSD misorientation analyses and an Excel spreadsheet of crystallographic calculations are available at https://doi.org/10.6084/m9.figshare.c.6710513

Mapping has, is and will play to occupy a core role in the geological sciences. Historically it contributed to the growth of geological understanding throughout the nineteenth and twentieth centuries, which arguably began with Smith (1815), although the influences of earlier and contemporary workers must not be excluded from any appreciation (e.g. see the review by Szaniawska 2018). Today, while traditional mapping continues to prove significant, especially as new ideas evolve to challenge previous perceptions, modern techniques have expanded the range of opportunities for map work. Such techniques include various satellite and bathymetry imagery that allow mapping in ever increasing detail of the Earth's terrestrial and submarine surfaces, while similar opportunities are increasing to map the planets and moons of the solar system (see contributions in this volume).

Perhaps a less appreciated geological *mapping* application is that on the microscopic scale. Within the spectrum of geological mapping, microstructures obviously fall towards the small-scale end of a potentially very large range of inter-connected scales. Figure 1 is a conceptual model that illustrates this range of scales based on the location of the sample used in this contribution, which is from the Eriboll Sandstone Formation in the Assynt region of NW Scotland. The figure also provides a relatively simple overview of the geological context of the sample, both spatially and temporally.

The smallest scale of mapping illustrated (Fig. 1a) relates to the crystal structure of quartz and provides the physical basis for indexing quartz electron backscattered diffraction (EBSD) patterns. This 'spherical electron diffraction map' (Lloyd and Ferguson 1986) is a representation of the quartz trigonal crystallographic unit triangle. It was constructed on a 53 cm diameter sphere by merging individual diffraction patterns obtained from oriented samples cut from a quartz single crystal (Fig. 1b), scaled appropriately according to the individual angular spread of the patterns (*c.* 15° relative to the whole unit triangle).Note how the single crystal and spherical map relate to each other via the indexing of specific crystal faces and/or directions. The spherical electron diffraction map (Fig. 1a) involves two superposed scales. First is the spherical crystallographic unit triangle, defined by the 90° from the

From: Butler, R. W. H., Torvela, T. and Williams, L. (eds) *Geological Mapping of Our World and Others.* Geological Society, London, Special Publications, **541**,
https://doi.org/10.1144/SP541-2022-332

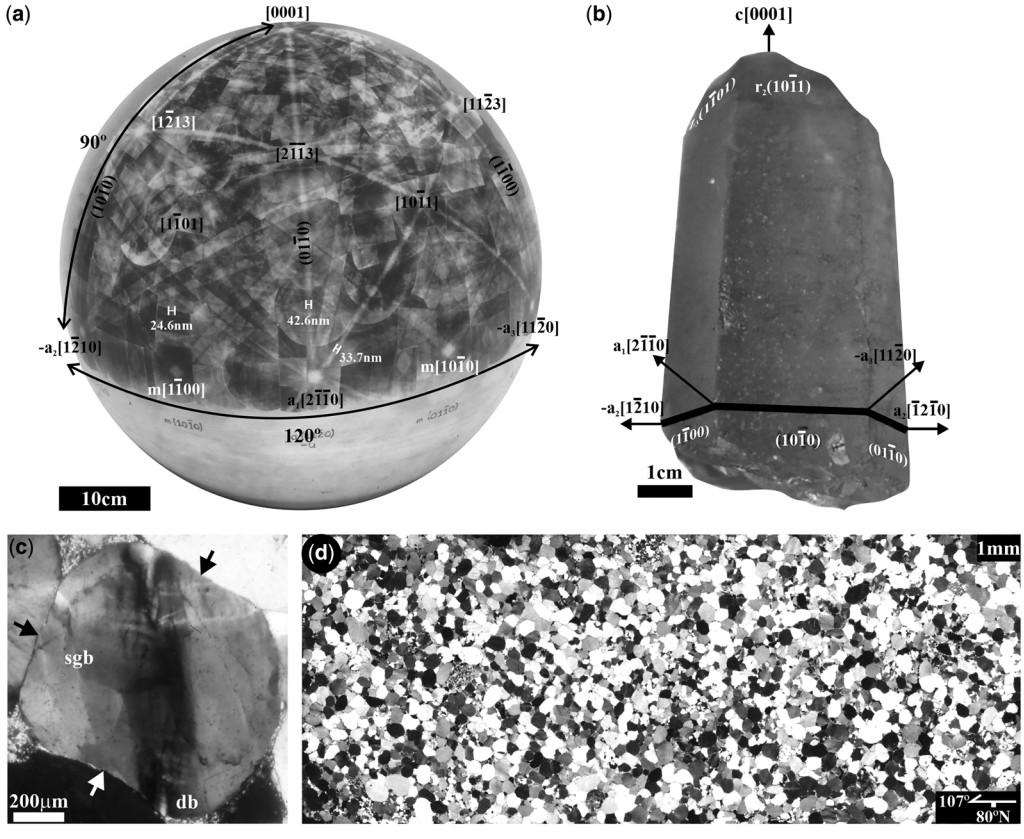

Fig. 1. Examples of scales of mapping based on the location of the sample used in this study (Skiag Bridge, Assynt, NW Scotland). (**a**) Spherical electron diffraction 'map' of quartz crystal structure (Lloyd and Ferguson 1986). (**b**) Individual quartz single crystal. (**c**) and (**d**) Crossed-polar optical images of individual quartz grain (sgb, subgrain boundary; db, deformation band; arrows, stress concentrations) and sample thin section respectively. (**e**) Field photograph of Skiag Bridge back-thrust fault with sample location. (**f**) Sampling and measurements 'map' of the fault zone (Knipe and Lloyd 1994). (**g**) BGS 1:50 000 scale map of Assynt. (**h**) 1:20 00 000 scale map of Caledonian orogeny in NW Scotland (Thigpen *et al.* 2010). (**i**) Schematic plate reconstruction scale map at the end of the Caledonian orogen (Chew 2005). (**j**) Planetary scale map of Earth geography after Grampian Orogeny (*Earth Viewer*).

c[0001] axis to the basal plane and 120° along the basal plane between two $+a\langle 11\bar{2}0\rangle$ axes. Second, the width of the individual diffraction bands in the patterns and on the map is inversely proportional to the spacing between the relevant adjacent lattice planes; for example, the spacings of the $(11\bar{2}0)$, $(01\bar{1}0)$ and $(01\bar{1}\bar{1})$ lattice planes are 24.6, 42.6 and 33.7 nm, respectively.

The conventional method of viewing the microstructures of geological samples on the grain scale is by plane- or cross-polarized optical microscopy of thin sections. Examples of such optical 'maps' are shown in Figure 1c (individual grain scale) and Figure 1d (whole sample thin-section scale). However, numerous modern technological developments today provide opportunities for alternative representations of microstructures. This contribution makes use of the scanning electron microscope (SEM) and in particular various imaging modes based on EBSD (see below for examples). Typically, the 'thin-section' scale of maps is obtained from 'hand-specimen' scale samples collected from individual field locations. In terms of the sample studied here, it forms part of a suite of samples collected from the Skiag Bridge back-thrust fault (Fig. 1e), Assynt (Knipe and Lloyd 1994; Lloyd 2000). Figure 1f is a 'location map' of the samples collected, which also includes relevant field measurements.

The subsequent increases in scale involve conventional geological map representations. Firstly, the immediate environs of the sample locality within

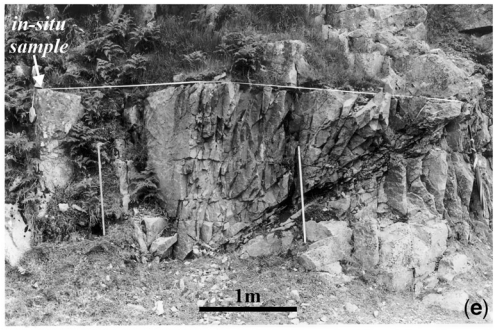

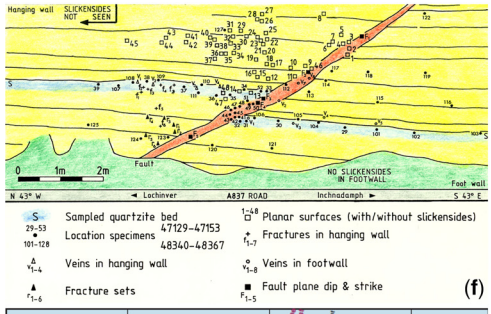

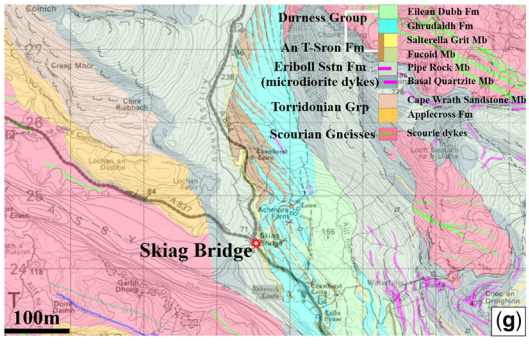

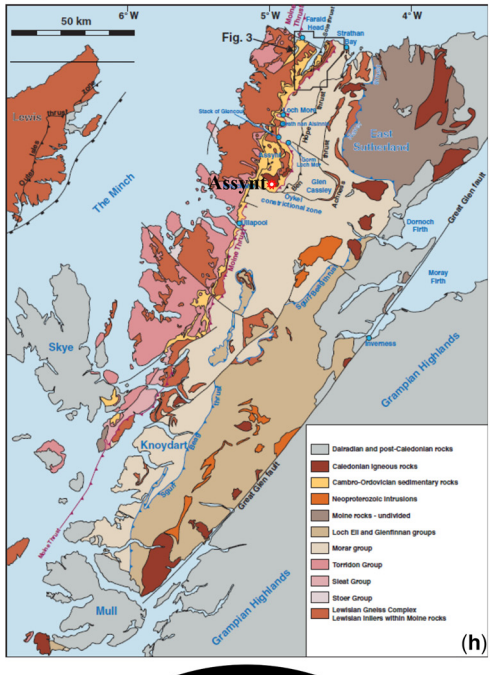

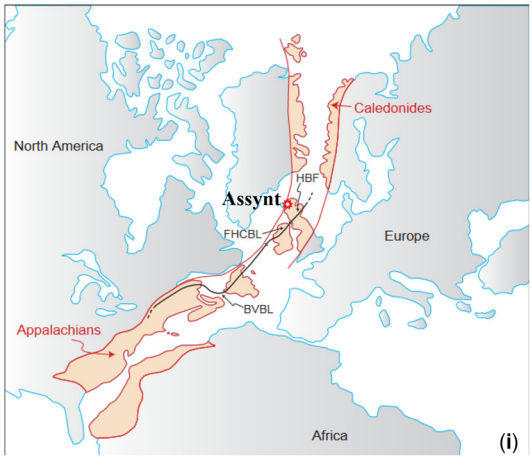

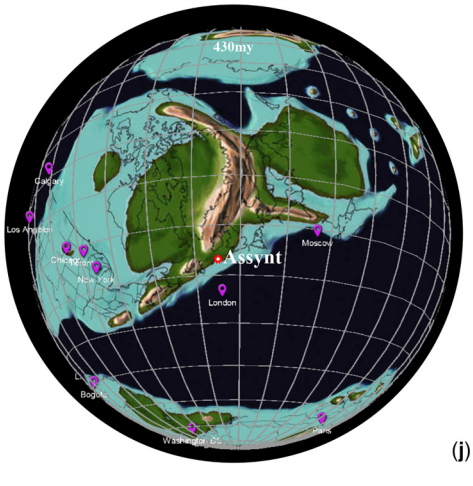

Fig. 1. *Continued.*

the adjacent foreland to the Moine Thrust Zone in Assynt are shown by the appropriate British Geological Survey (2007) map; in the example shown this is at 1:25 000 scale (Fig. 1g). Further increases in scale show maps of the whole NW Scotland Caledonides (e.g. Thigpen *et al.* 2010) at 1:20 00 000 (Fig. 1h) and then the whole Grampian orogeny (e.g. Chew 2005) at *c.* 1:100 000 000 (Fig. 1i) scales. Finally, the location of the Skiag Bridge sample can be viewed on the plate tectonics planetary scale of *c.* 1:150 000 000 (Earth Viewer), for example imagining the situation during the Silurian at the end of the Grampian Orogeny (Fig. 1j). Figure 1 therefore represents related 'maps' that cover *c.* 17 orders of magnitude in terms of scale to provide a holistic summary of the geological framework.

This contribution considers the 'mapping' of intragranular microstructures developed in quartz via SEM–EBSD, now recognized as one of the principal modern techniques for investigating rocks and minerals on the micro-scale (e.g. Dingley *et al.* 2018). In this technique, an electron beam is scanned across a sample to progressively acquire electron backscatter diffraction patterns, from which crystal orientations at the sub-micron scale can be determined (e.g. Dingley 1987). The patterns are indexed simultaneously and automatically (e.g. Wright and Adams 1992) at rates of up to several thousand per second on modern SEM, allowing whole samples equivalent in size to conventional thin-sections to be analysed quickly, efficiently and accurately. Thus, SEM–EBSD not only makes it possible to 'map' microstructures based on various criteria (e.g. phase, crystallography, physical properties) at the scale of the thin-section (Fig. 1d), individual grain (Fig. 1c) and significantly smaller (e.g. Fig. 1a), but also facilitates upscaling (e.g. Fig. 1e through to potentially Fig. 1j) where necessary and/or appropriate.

The crystal orientation information obtained via SEM–EBSD can be used to determine a wide range of material properties that are functions of the crystal structure. As well as the essentially ubiquitous crystallographic preferred orientation (CPO) and misorientation distributions, elastic (e.g. Young's modulus) and seismic (e.g. velocities and anisotropies) properties are readily determined. These results can also be displayed as various types of 'maps' based fundamentally on the spatial variations in the crystal orientations (e.g. Adams *et al.* 1993), providing a modern version of the optical axis distribution analysis introduced by Sander (1950). However, SEM–EBSD mapping requires not only accurate definitions of crystal orientation (variations) on the (sub-)micrometre scale but also the complete orientation of the boundaries that separate domains of (slightly) different orientations (e.g. subgrains). While the former is readily achieved, the latter has conventionally proved problematic. Boundary orientation determination has usually relied on EBSD misorientation analysis. Unfortunately, it will be shown that misorientation is an incomplete definition of boundary orientation. A recently developed practical method based on 'plane matching' is therefore employed to determine the complete ('five-parameter') orientation of intragranular boundaries (Lloyd *et al.* 2021).

The contribution begins with a brief description of the (crystallographic) background behind the definition of (intragranular) boundaries, before providing a summary of the new boundary orientation determination method. It therefore expects some understanding of crystallography, such as the definition, expression and relationship between crystal planes and directions in general and in the quartz trigonal crystal system in particular. An interactive Excel spreadsheet provided in the Supplementary material is available to assist with this understanding. Next, the orientations of intragranular boundaries in an individual quartz grain are mapped via a combination of SEM–EBSD and the new boundary orientation method. Finally, the implications of the 'boundary mapping' are discussed, particularly in terms of the analysis and interpretation of quartz intragranular boundaries in general and Dauphiné twins in particular, which involves some understanding of the basic principles of three-dimensional stress evolution and representation via Mohr Circle analysis.

Background

Boundary orientation

Polycrystalline materials exhibit a range of boundary types that exist both between and within individual grains. While intergranular boundaries simply separate grains of the same phase, intragranular boundaries are more disparate. Probably the most common are subgrain boundaries but other types exist, such as deformation lamella, deformation bands and particularly twin boundaries. However, compared with the investigation of the regions separated by intra- and inter- granular boundaries, relatively little attention has been paid to the actual boundaries. One of the main reasons for this deficiency is the inherent difficulty involved in defining the precise orientation of the boundary plane. Nevertheless, the characteristics (e.g. energy, mobility, chemistry) of boundaries vary and impact critically on many material properties and processes of microstructural evolution.

In general, the definition of boundary orientation involves five parameters or degrees of freedom. Three parameters are required to describe the difference in orientation, or more appropriately misorientation, of the crystal lattices on either side of the

boundary. The conventional solution to this problem is provided by the misorientation angle/axis pair θ/[$uvw(t)$] (Fig. 2a), or the angle θ (one degree of freedom) required to rotate one lattice into parallelism with the other about a specific axis [$uvw(t)$] in Miller (Bravais) notations (2 degrees of freedom), which can be described by a rotation transformation matrix (g_m),

$$\{g\}_m = \{C_i\}\{C_j\}^{-1} \quad (1)$$

where $\{C_i\}$ and $\{C_j\}$ are the respective adjacent crystal coordinate systems (e.g. Mainprice *et al.* 1993; Lloyd *et al.* 1997; Randle 2003). A further two parameters are required to define the orientation of the boundary plane, typically in terms of its normal direction (Fig. 2b). Thus, the complete orientation of intragranular boundaries involves five independent parameters (e.g. Sutton and Balluffi 1995; Randle 2006; Rohrer and Randle 2009; Sutton *et al.* 2015). The term disorientation is also used to mean the smallest physically possible rotation that will connect two orientations; the choice of rotation angle arises because of crystal symmetry considerations (e.g. Randle 2003, 2006).

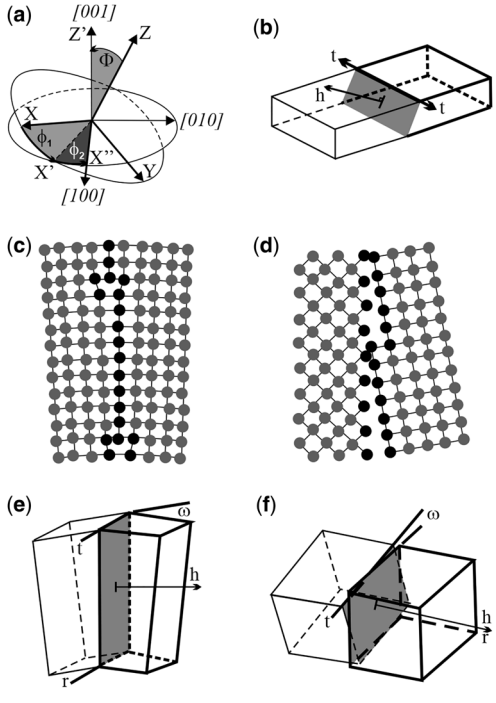

Fig. 2. Boundary relationships. (**a**) Definition of the crystallographic orientations of two adjacent domains and the three rotations (ϕ_1, Ψ, ϕ_2) required to bring their respective lattices XYZ and X′Y′Z′ into coincidence, as represented by the misorientation angle/axis pair, θ/<uvw>. Note that the rotation angle is the same as the misorientation angle. (**b**) Two adjacent domains share a common boundary plane, with trace (t) and normal (h). (**c**) Schematic structure of an intragranular (high angle grain) boundary. (**d**) Schematic structure of an intergranular (low angle grain) boundary. (**e**) Pure tilt boundary: note, as the common boundary rotation axis (r) is parallel to t and normal to h, the rotation angle (ω) and axis pair are defined by ω<uvw>. (**f**) Pure twist boundary: as r is parallel to h and normal to t, the rotation angle/axis pair is again defined by ω<uvw>.

The distinction between intra- and inter-granular boundaries is in their misorientation angles (e.g. Humphreys and Hatherly 2004) and follows from the dislocation structure of boundaries (Read and Shockley 1950). The distinction leads to the terms low-angle 'grain' boundaries (LAGBs) or subgrains and high-angle grain boundaries (HAGBs). In general, LAGBs consist of isolated dislocations (Fig. 2c) such that their structure and properties vary as a function of misorientation (e.g. Humphreys and Hatherly 2004). However, as dislocation density, and hence misorientation, increases, the dislocation separation decreases until the dislocation cores overlap and the ordered structure of the boundary breaks down (Fig. 2d), resulting in large excess free energies. A further consequence of this dislocation behaviour is that the misorientation angle is more influential in terms of impact on material properties for LAGBs than for HAGBs (e.g. Humphreys and Hatherly 2004). The precise angle for the change from LAGBs to HAGBs is variable and depends on a number of factors (e.g. composition, crystal structure, bonding) that influence the dislocation network; it is to some extent also dependent on what properties of the boundary are of interest. A typical range of values is from 10 to 15° (e.g. Doherty *et al.* 1997). The critical angle for quartz appears to be approximately 10° (e.g. White 1977; Valcke *et al.* 2006). While EBSD studies of misorientation angle/axis pairs are potentially justified in ignoring the orientation of the boundary plane normal, at least in terms of intragranular boundaries, they are nevertheless incapable of distinguishing specific boundary types.

Boundary types

While there are a number of ways to describe boundaries, the traditional method uses the tilt/twist description (e.g. Sutton and Balluffi 1995). This method considers that there are two ideal types of boundaries: pure tilt and pure twist. Pure tilt boundaries (Fig. 2e) develop by the progressive addition of, in principle, a single set of edge dislocations to achieve the misorientation between adjacent domains (e.g. Read and Shockley 1950). A rotation angle (ω) and axis (r) can therefore be recognized. As the rotation axis lies within the boundary plane

and hence perpendicular to the boundary plane normal (h),

$$r \cdot h = 0 \quad (2)$$

Pure twist boundaries (Fig. 2f) develop via (at least) two sets of (not necessarily orthogonal) screw dislocations to achieve the misorientation between adjacent domains (e.g. Read and Shockley 1950). The rotation axis is now perpendicular to the boundary plane and hence parallel to its normal, such that,

$$r \cdot h = 1 \quad (3)$$

However, in practice most boundaries are combinations of the tilt and twist components necessary to create the 'best-fit' between adjacent domains. Thus,

$$0(\text{pure tilt}) \leq \text{TTC} \leq 1(\text{pure twist}) \quad (4)$$

where TTC is the vector product of the rotation axis (r) and boundary plane normal (h) and is known as the boundary tilt–twist component index (Amouyal *et al.* 2005). In each of these definitions it is important to recognize that the tilt or twist angle is not necessarily the same as the misorientation angle, although for low angle boundaries they are often the same.

In spite of the apparent simplicity of these equations, boundary configurations are often much more complex. In particular, boundary surfaces can be either planar or curviplanar in three dimensions, although the latter may comprise planar segments (i.e. facets). If the grain boundary is curved the two parameters characterizing the grain boundary plane become functions of position within the curviplanar surface. In fact, many boundaries, especially in materials that have undergone recovery, are effectively planar. In contrast, boundaries formed in materials owing to deformation and recrystallization where boundary migration is active are typically curved, with the curvature providing the strain energy that drives boundary mobility. The approach taken in this contribution applies to planar boundaries. However, it may be adapted to curviplanar boundaries, either by resolving them into planar segments and/or by recognizing any facets. Nevertheless, a planar boundary separating two adjacent misoriented crystal lattice domains can have an effectively infinite number of physical orientations (Fig. 2b, e & f).

To distinguish these physical orientations requires definition of the boundary plane normal direction. While the misorientation angle/axis pair is readily determined, particularly today via SEM–EBSD, determination of the boundary plane normal direction has proved a much more difficult proposition. This is because of the fact that while boundaries are inherently three-dimensional features, typically only their two-dimensional intersection with a surface plane is observed. Methods do exist to measure the orientation of boundary planes (e.g. optical microscopy universal stage, transmission electron microscopy, focused ion beam, X-ray and neutron techniques), but they tend to be restrictive, laborious, complex and/or expensive (e.g. Rohrer and Randle 2009). Recently, Lloyd *et al.* (2021) proposed a practical method to determine the complete five-parameter orientation of intra- and (some) inter-granular boundaries.

'Plane matching' method

The complete method for the determination of intragranular boundaries is described in Lloyd *et al.* (2021). Here we provide the main details in stepwise progression (1)–(11), illustrated in Figures 3 and 4, with Figure 3a providing the basic quartz crystallography for reference (note the shaded region defining the trigonal crystallographic unit triangle).

(1) The method proposed by Lloyd *et al.* (2021) is based on initial observations made using the SEM electron channelling (EC) technique (e.g. Lloyd 1987). Figure 3b is a spherical electron channelling pattern (ECP) map (Lloyd and Ferguson 1986; see also Day 2008, 2009), equivalent to the unit triangle shown in Figure 3a. ECP maps are analogous to EBSD patterns; however, they typically cover a smaller angular spread (e.g. *c.* 20° compared with up to *c.* 100°), although exhibiting more diffraction detail. In addition, and similar to EBSD, there is an equivalent EC image based on sample crystallography (Fig. 3c), originally known as orientation contrast but now more familiarly as electron or orientation channelling contrast imaging (e.g. Zaefferer and Elhami 2014).

(2) The EC crystallographic orientation contrast image in Figure 3c shows a quartz grain with a prominent intragranular boundary separating two domains, A and B. One aspect of EC is that a one-to-one relationship exists between each point in the sample surface and its equivalent in the ECP. ECP maps are formed by rocking an incident electron beam about a fixed point on a sample surface, the diameter of the ECP being equal to twice the rocking angle. If the electron beam is rocked about a point on a boundary (e.g. Fig. 3c), 'partial' ECP maps are obtained from each side separated by the trace of the boundary (Fig. 3d). The displacements exhibited by equivalent variously oriented EC bands are determined by the nature of the

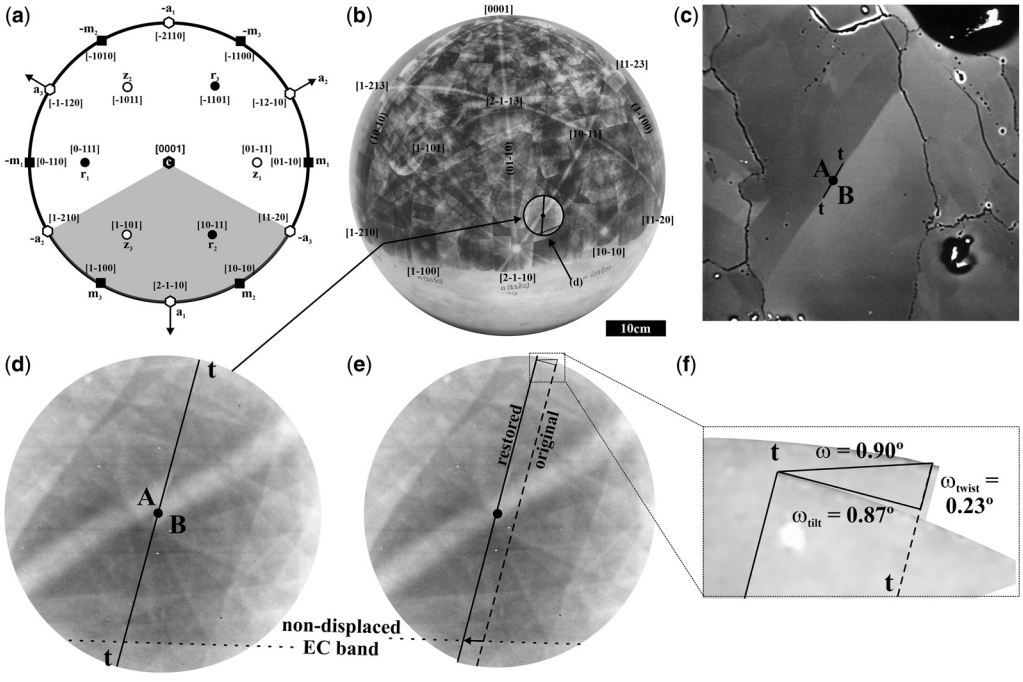

Fig. 3. Boundary orientation method 1: electron channelling (EC) basics. (**a**) Quartz crystallography; shading indicates the crystallographic unit triangle (inverse pole figure). (**b**) Quartz spherical electron channelling pattern (ECP) map covering the unit triangle (Lloyd and Ferguson 1986). (**c**) EC crystallographic orientation contrast (OC) image of a quartz grain with a prominent intragranular boundary separating domains A and B. (**d**) Partial ECP maps from either side of the boundary in (**c**) imaged by rocking the incident electron beam about a point on the boundary (diameter = twice the rocking angle, RA, =15°); the location of patterns in the quartz unit cell (**b**) is indicated. The boundary trace (*t*) displaces all but one EC band (lattice plane), which must therefore be normal to the boundary rotation axis. Note, rotation of boundary trace caused by switching from OC to ECP modes (**e**) Displacement of EC bands removed by translating one partial pattern (B) relative to the other (A) parallel to the matched plane EC band (**f**) Determination of boundary rotation angle (ω), including its boundary normal tilt (ω_{tilt}) and boundary parallel twist (ω_{twist}) components, via restoration of the partial ECP maps to their original and equivalent configurations (**e**).

boundary. However, an EC band that is not displaced across the boundary (Fig. 3d) must not only contain the boundary translation vector but also be normal to the rotation axis (*r*) involved in boundary formation (Fig. 2b, e & f).

(3) Pumphrey (1972) referred to the identification of a non-displaced diffraction band as 'plane matching', recognizing that periodic lines observed in TEM images of HAGBs result from the mismatch of either low or higher index atom planes across the grain boundary. However, the 'plane matching' approach specifically does not determine the orientation of the grain boundary plane; rather, it constrains the direction of growth or migration of one grain (boundary) at the expense of another grain (e.g. during recrystallization). Watanabe (1983) and Watanabe *et al.* (1989) reported ECP observations of grain boundaries that supported the 'plane-matching' model, which led them to suggest that ECP provided a powerful tool to determine the relative orientation relationship between adjacent grains that geometrically characterize a grain boundary (see Lloyd *et al.* 2021, Fig. 13). From here on in, the non-displaced diffraction band of Lloyd *et al.* (2021) is referred to as the 'matched plane' and its identification as 'plane matching'. For the moment, the 'matched plane' is recognized manually by visual inspection of either EBSD patterns and/or spherical Kikuchi maps (see below). The 'matched plane' provides not only the bi-directional boundary migration vectors via its 'strike' orientations but also the boundary rotation axis (*r*) via its normal orientation (Fig. 3d).

(4) By translating one of the partial ECP maps parallel to the matched plane until the original

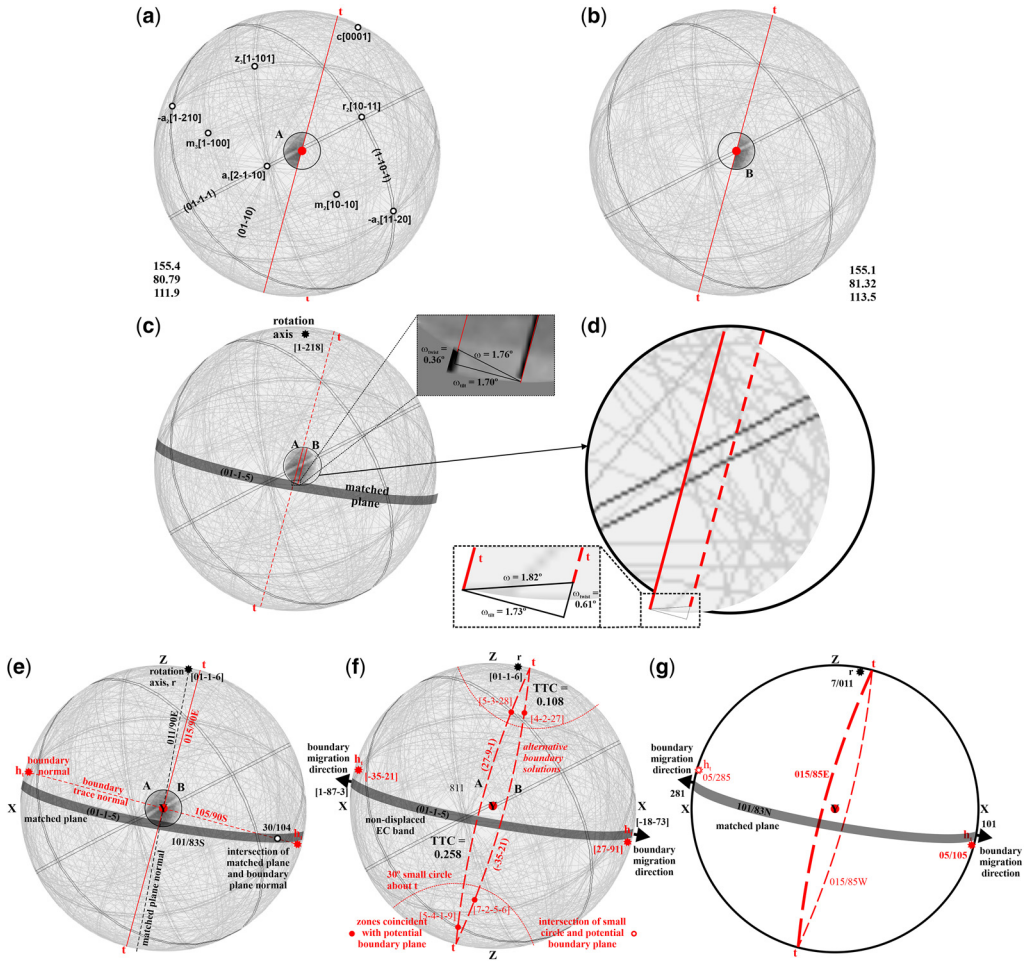

Fig. 4. Boundary orientation method 2: adaption to electron backscattered diffraction (EBSD). (**a**) and (**b**) Partial ECP maps from either side of an intragranular boundary projected within the framework of orthographic spherical Kikuchi maps (SKMs); note their respective Euler angle triplets. (**c**) Partial SKM for each side of the boundary trace fitted together by translation parallel to the matched plane to remove the effect of the boundary; *inset*, detail of fitting and determination of total and tilt/twist components angular rotations. (**d**) Simulation of partial ECP maps by enlargement of SKMs within the rocking circle (diameter 15°); *inset*, calculation of rotation angles. (**e**) Spherical geometry orientations of boundary trace (assumed initially to represent a vertical plane), the matched plane, their vertical normal planes, the rotation angle (normal to matched plane) and the intersection of the boundary trace normal and the matched plane. (**f**) Determination of alternative boundary orientations from intersections of the matched plane vertical normal with the small circle about the trace (t) defined by the plunge of the intersection of the trace normal and the matched plane; each solution has a tilt–twist component (TTC) value that defines the boundary type. The choice between the alternative orientations is constrained by the nearest (sub-)parallel low-index lattice plane to one of the great circles identified in the SKM. (**g**) Summary of boundary orientations in terms of stereographic projection.

pattern configuration is restored (Fig. 3e), the effect of the boundary can be removed. By measuring the displacement distance and using the internal scaling present in the ECP owing to the rocking angle, the rotation angle (ω) of the boundary can be determined (Fig. 3f). The boundary plane (normal) rotation axis is therefore defined by ω/r or $\omega/[uvw(t)]_r$ in Miller (Bravais) notations.

(5) As most boundaries are general in nature, the displacement vector will tend to be oblique to the boundary trace. The tilt (ω_{tilt}) and twist (ω_{twist}) components normal and parallel to the boundary can therefore be determined

by measuring the perpendicular and parallel displacements accordingly (Fig. 3f), from which the boundary TTC can be calculated from equation (2).

(6) Steps 1–5 illustrate the EC basis of the boundary orientation determination method. To facilitate complete boundary orientation determination and to allow application of the method involves use of spherical Kikuchi maps (SKMs) and adaption of the basic method to EBSD data (Lloyd *et al.* 2021). To illustrate this adaption, Figure 4a and b shows the partial-ECP maps (Fig. 3d) projected within the framework of the quartz SKM, which also allows their Euler angle triplets to be determined. Note that SKMs involve orthographic or gnomonic projections.

(7) Next, the partial SKMs for each side of the boundary trace are fitted together by translation parallel to the matched plane to remove the effect of the boundary (Fig. 4c). Alternatively, the regions of the SKM within the rocking circle representing the partial ECP maps can be enlarged and then fitted together by translation parallel to the matched plane to remove the boundary effect, after which the total, tilt and twist angular rotations can be determined as before (Fig. 4d and inset).

(8) So far, only the boundary angular rotation and its tilt and twist components have been determined, either from partial ECP maps (Fig. 3d–f) or EBSD and SKMs (Fig. 4a–d); the orientation of the boundary normal has not been considered. Achieving this orientation involves representing the boundary trace and matched plane in terms of their spherical geometry orientations (i.e. strike, dip and sense); note, although the boundary trace is a linear element, it is assumed initially to represent the intersection of a vertical plane with respect to the specific projection (Fig. 4e). In addition, the (vertical) normal planes to the trace and the matched plane are similarly defined, while the rotation axis (matched plane normal) and the intersection of the boundary trace normal and the matched plane are represented in terms of their plunge and azimuth.

(9) The pitch of the intersection of the boundary trace normal and the matched plane defines a small circle centred on both ends of the boundary trace (Fig. 4f). The boundary plane must join the two ends of the trace by passing through the small circle. In addition, the boundary plane is constrained by spherical geometry to pass through the intersection of the small circle and the vertical plane normal to the matched plane. There are only two possible alternative great circle solutions, symmetrical about the trace (Fig. 4f). The choice between the alternative orientations is constrained by the nearest (sub-)parallel low-index lattice plane to one of the great circles identified in the SKM.

(10) To depict boundary orientations in terms of crystallography involves comparison with the SKM (Fig. 4f, g). The indices of the boundary plane can be accurately determined from pairs of crystal poles that lie on the plane, again identified from the SKM, via standard crystallographic relationships (Fig. 4g). Similarly, the normals to both the boundary and matched planes (i.e. the rotation axis) can be determined via standard crystallography.

(11) Having determined the boundary plane normal and rotation axis orientations, the type of boundary can be recognized from the TTC value determined via equation (3).

Implications of plane matching method

Steps 1–11 above summarize the method devised by Lloyd *et al.* (2021) to determine the five parameters needed to characterize fully the orientation of (intragranular) boundaries. The method was tested on various intra- and inter- granular boundaries in olivine. The test results raised some interesting observations. Perhaps the most significant of these is the comparison between the rotation angle/axis pair $\omega/[uvw(t)]_r$ determined by the new method and the misorientation angle/axis pair $\theta/[uvw(t)]$ obtained from conventional EBSD analysis. In general, the two angle/axis pairs were different.

The difference between misorientation and rotation angle/axis pairs highlights an important aspect of misorientation analysis, namely that the crystallography of an interface is only partially specified by the misorientation (e.g. Randle 2006). Indeed, in the initial SEM/EBSD implementations of misorientation analysis (e.g. Mainprice *et al.* 1993; Lloyd *et al.* 1997; Wheeler *et al.* 2001), there was no requirement for two crystal lattices to share a common boundary (i.e. 'correlated' and 'uncorrelated' boundaries). Furthermore, depending on crystal symmetry, misorientations (or orientations) can be expressed by several different misorientation angle/axis pairs owing to the multiplication of the misorientation matrix by symmetry operators. Convention decrees that the pair with the lowest misorientation angle (θ_{min}) is chosen to represent the boundary *dis*orientation (e.g. Randle 2004).

One of the examples described by Lloyd *et al.* (2021) is an olivine grain with a segmented boundary comprising almost pure tilt and general components; however, as the Euler angle triplets remain constant along each side of the boundary, the misorientation

angle/axis pair is also constant. In contrast, the segments exhibited different boundary rotation angle/axis pairs, which additionally classified the boundary types via TTC as almost pure tilt and general with approximately equal tilt and twist components. It is clear therefore that misorientation analysis and boundary rotation angle/axis pairs are not (necessarily) the same. Misorientation is the active rotation required to rotate one set of crystal axes into coincidence with another based on a fixed reference frame, usually one of the crystals (e.g. Fig. 2a), and provides only three of the five degrees of freedom. In contrast, all five degrees of freedom can be defined by two pairs of parameters, one for each side of the boundary plane, plus a twist angle between the two crystal lattices (e.g. Fig. 2e, f), often referred to as the tilt–twist description. Consequently, the tilt–twist (boundary rotation) angle is not necessarily the same as the misorientation angle, although it can be (e.g. pure tilt and pure twist boundaries; Liu *et al.* 2005). *Thus, conventional (EBSD) misorientation analysis and the plane matching method* (Lloyd *et al.* 2021), *which incorporates the tilt–twist definition, should not necessarily be expected to provide identical solutions for the same (intragranular) boundary*.

As conventional (EBSD) misorientation analysis is insensitive to boundary type, it follows that boundaries with the same misorientation can have different boundary plane orientations. Thus, care is required when estimating physical properties that depend on one or other of these measures. In general, the proportion and distribution of boundary types (i.e. tilt, twist, general) control boundary network properties (e.g. Liu *et al.* 2005); for example, boundaries with the same misorientation but different boundary plane orientations may have very different energies, such that the disorientation angle is not a good predictor of boundary energy (e.g. Rohrer 2011). Nevertheless, boundaries in polycrystals are commonly categorized by their misorientation, leading to the coincidence site lattice (CSL) classification for particular combinations of misorientation axis/angle based on the inverse density of coincident lattice sites (Σ).

CSL is a widely accepted parameter used to investigate correlations between geometry and the physical properties of boundaries (e.g. Wolf and Lutsko 1989). However, while ideal boundaries are planar defects, CSL relates only to lattice misorientations. Approaches that measure orientations of boundary planes have been typically technically challenging (e.g. Randle *et al.* 1999; Randle 2001). One such approach is to determine the nearest lowest-index boundary (normal) axis solution to define the misorientation between adjacent lattices (e.g. Gourdet *et al.* 1998). The two approaches are not equivalent and it has been suggested (e.g. Cross and Randle 2003) that an unambiguous analysis of intragranular boundary orientation involves consideration of the low-order coincident axial direction solution, including visualizations of boundary geometry (e.g. Warrington and Boon 1975), rather than just the disorientation and hence coincident lattice sites.

To summarize this section in terms of implications for microstructural mapping, it is important to recognize that such mapping is based on variations in crystal orientation, whether within or between individual grains. Regions of effectively constant crystal orientation are separated by boundaries that are conventionally defined in terms of lattice misorientation. This definition is clearly insufficient to fully characterize and hence map boundaries completely. We therefore choose to map intragranular microstructures using EBSD to determine crystal orientation on the (sub-)micron scale and then employ the plane matching method to accurately define the orientations and types of boundaries present. Obviously, the EBSD data can also be used to determine the mis/dis-orientation of the boundaries.

Results

Sample details

The sample considered (47139A of Knipe and Lloyd 1994; see Fig. 1c, d) is from the Pipe Rock Member of the Cambrian Eriboll Sandstone Formation (e.g. Swett 1969), at Skiag Bridge, Assynt, NW Scotland (UK grid reference NC23552431). It was collected from the vicinity of a minor back-thrust fault developed in the immediate foreland to the Moine Thrust Zone (e.g. Lloyd and Knipe 1992; Knipe and Lloyd 1994; Lloyd 2000), although Coward (1984, 1985) recognized a structurally lower 'sole thrust' with a displacement of *c.* 3 km along the course of the Skiag Burn. The Skiag Bridge back thrust occurs in the hanging wall of the latter feature and has accommodated *c.* 1 m of displacement on a *c.* 30 cm wide displacement zone, although an adjacent damage zone is observed in both the hanging wall and footwall (Knipe and Lloyd 1994). Maximum deformation conditions in the Assynt region have been estimated at temperatures of 200–250°C, pressures of 200–300 MPa and hence depths of 6–9 km depth (Johnson *et al.* 1985; Knipe 1990), while re-evaluation of the temperatures in the foreland at Skiag Bridge based on microstructures (e.g. Fig. 1c, d) and authigenic quartz cement revealed by cathodoluminescence (e.g. Lloyd and Knipe 1992) suggests a maximum upper limit of 200°C.

The sample was collected from just outside of the fault deformation zone visible in the field (Fig. 1e, f), where bedding dips shallowly towards the ESE. We therefore consider it to have experienced few Skiag Bridge back thrust fault-related deformation effects

(Knipe and Lloyd 1994; Lloyd 2000). The chosen sample was cut normal to bedding and parallel to the dip direction, such that X is parallel to bedding dip, Y is parallel to bedding strike and Z is normal to bedding. It is emphasized that X, Y and Z are unrelated to the kinematic reference frame of the Skiag Bridge back-thrust fault. The sample is comprised of rounded but somewhat poorly sorted sedimentary grains up to *c.* 1 mm in size (Fig. 1d).

EBSD mapping

The conventional EBSD map is known as 'All Euler' and is based on the values of the Euler angle triplets (Fig. 2a) that define the crystal orientation from point to point. The separation distance between points is known as the step size and is chosen depending on the mapping objectives. To get a detailed representation of the sample microstructure (e.g. equivalent to an optical thin-section such as Fig. 1c, d) requires a small step size (e.g. few to sub microns) and concomitantly long analytical times (perhaps up to several days) depending on the area analysed. Fortunately, modern EBSD systems are capable of analysing hundreds to thousands of EBSD patterns per second depending on phase, drastically reducing analytical times and making large area mapping eminently feasible.

Figure 5a is an EBSD All Euler map of the sample. Note that it is not the same sample as that shown in the thin-section image (Fig. 1d) as it is a solid block, which allows for better sample preparation, cut parallel to the thin section. Nevertheless, the EBSD map shows the same sedimentary features of rounded but somewhat poorly sorted sedimentary grains up to *c.* 1 mm in size. However, while the thin-section crossed-polars image is based only on the orientation of the quartz optic or c[0001] axis, the EBSD All Euler image is based on the full crystal orientation at each analytical point. It is therefore much more sensitive to changes in crystal orientation between and particularly within grains, with images colour-coded accordingly. Perhaps the most significant feature observed in the quartz All Euler EBSD maps is the presence of significant Dauphiné twinning (Fig. 5a). As Dauphiné twinning involves a 180° (symmetrically equivalent to 60°) rotation about c[0001], it cannot be observed in optical crossed-polars images (Fig. 1c, d). The twins have characteristic irregular and variably oriented outlines and typically appear to penetrate into grains from grain boundaries (Fig. 5a). Numerous EBSD studies of quartz have revealed the ubiquity of Dauphiné twinning in both sedimentary and tectonic situations (e.g. Lloyd 2004; Mørk and Moen 2007; Menegon *et al.* 2011). A complementary EBSD map ('Euler 3') based on the variation of the third Euler angle, which involves rotation about the quartz *c*-axis, emphasizes the Dauphiné twin microstructure in terms of distinctly lighter/darker intragranular regions compared with the contrast of the parent grain (Fig. 5b).

The individual crystal orientations defined by the EBSD Euler angles triplets can also be represented in terms of 'pole figures' to describe the CPO. For quartz, the conventional pole figures considered (Fig. 5c) are for c[0001], $a\langle 11\bar{2}0\rangle$, $m\langle 10\bar{1}0\rangle$, $r\langle 10\bar{1}1\rangle$ and $z\langle 01\bar{1}1\rangle$. As is to be expected for an essentially undeformed sedimentary quartz arenite, the CPO is generally dispersed and disorganized. However, there is an obvious positive first-order rhomb $r\langle 10\bar{1}1\rangle$ maximum located sub-parallel to the strike of bedding (i.e. Y), as well as a peripheral dispersion of *r*-poles sub-parallel to the XZ plane. This fabric is due to the presence of Dauphiné twinning (Fig. 5a, b), which forms under the application of stress concentrated loads, a process termed piezocrescence by Thomas and Wooster (1951).

All minerals are intrinsically anisotropic in their elastic properties, which therefore vary with crystal direction. In quartz, poles to more compliant crystal planes tend to align with the applied stress (e.g. Tullis and Tullis 1972). The variation in compliance is reflected in the variation in Young's modulus, which can be derived from the Euler angle triplets (e.g. Mainprice *et al.* 2011). Figure 5d plots the variation in Young's modulus for a quartz single crystal; note that the lowest values and hence most compliant directions are sub-parallel to $r\langle 10\bar{1}1\rangle$, which explains the *r*-maxima CPO in terms of Dauphiné twinning (e.g. Minor *et al.* 2018). It is also possible to 'map' the variation in Young's modulus (and other elastic properties such as Poisson's ratio and the shear and bulk moduli) over the whole sample (e.g. Fig. 5e). Values range from 69 to 130 GPa, although most grains tend towards the lower end, while the Dauphiné twinning components are clearly distinguished by distinct changes in colour.

In addition to the whole sample EBSD-based maps, a representative grain was also selected for detailed microstructural mapping via misorientation and plane matching methods. The grain (see Fig. 5 for its various representations) has a distinct subgrain microstructure, although this is not obvious in the All Euler (Fig. 5a) and Young's modulus (Fig. 5e) maps. It is somewhat clearer in the Euler-3 map (Fig. 5b), which reveals the presence of Dauphiné twins, but only in terms of the subgrain boundary traces. The most distinctive image of the subgrain microstructure is provided by the EBSD misorientation map (Fig. 5f); the equivalent map for the whole sample is also shown for comparison. However, while the misorientation map is very good for revealing the intragranular microstructure, neither it nor misorientation analysis can define the type and orientation of the

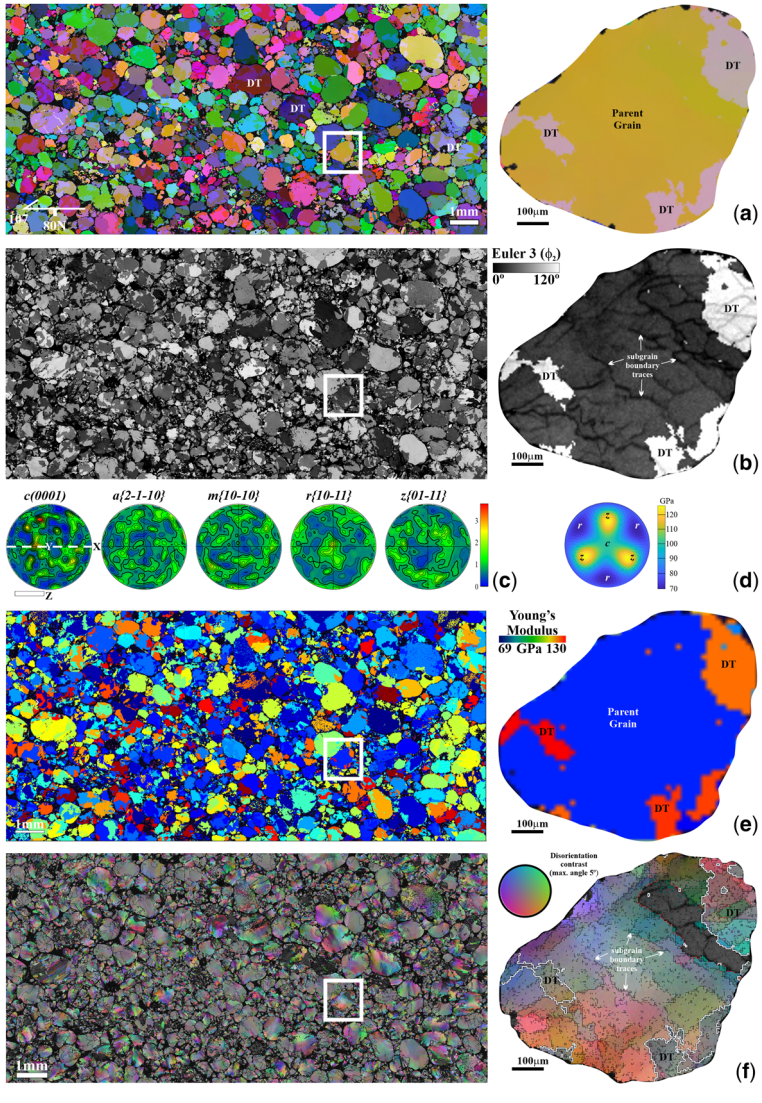

Fig. 5. Examples of EBSD-based mapping of the entire sample (left) and selected grain (right), indicated by white boxes; DT, Dauphiné twins. (**a**) All Euler. (**b**) Euler-3. (**c**) Crystallographic preferred orientation (CPO) pole figures: X, Y, Z parallel to bedding dip, strike and normal respectively; contours multiples of uniform distribution (m.u.d.). (**d**) Single crystal distribution of Young's modulus values. (**e**) Young's modulus. (**f**) Disorientation.

intragranular boundaries. For this, we resort to plane matching.

Plane matching boundary orientations

We now determine the five-parameter based orientations of boundaries in the grain selected from the sample (Fig. 5). The grain is shown in detail in Figure 6a, which is an EBSD misorientation map emphasizing subtle intragranular orientation differences and their intervening boundaries; also shown are the (numbered) boundaries analysed. This particular grain was chosen because its microstructure is representative of many grains in the whole sample (Figs 1d & 5a). In detail, there appear to be three distinct boundary regions present (Fig. 6).

(1) *Region A* comprises a background microstructure of small (e.g. *c.* 100 μm diameter), diffuse subgrains distinguished by their disorientation that occupies most of the grain. In general, subgrain boundaries are rather poorly defined (i.e.

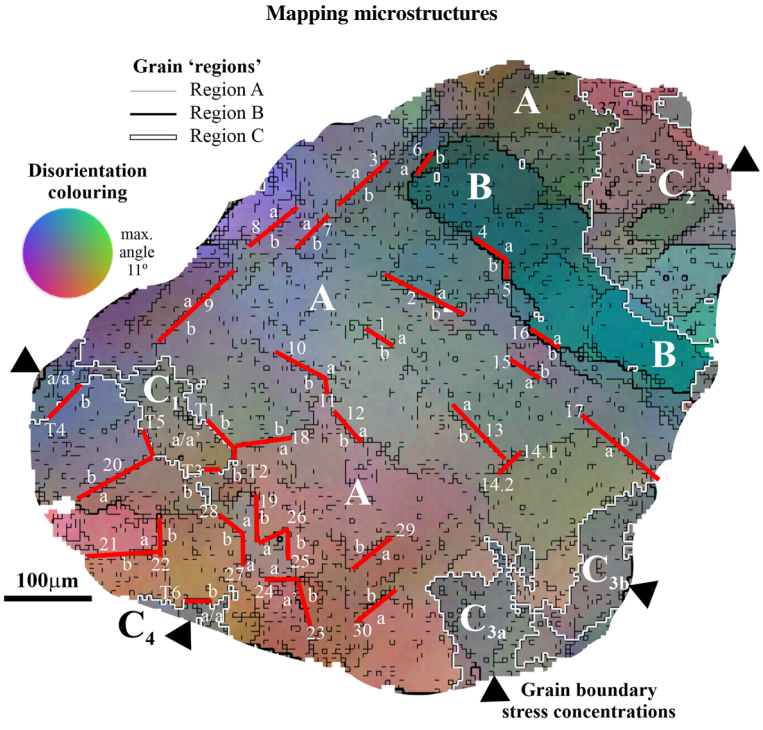

Fig. 6. EBSD disorientation map of the grain selected for plane matching analysis (see Fig. 5). Grain with regions (A–C) and subgrain boundaries analysed (numbered red lines) indicated (note, the associated symbols a and b merely distinguish each side of an individual boundary and have no other significance). Many subgrain boundaries are rather poorly defined (i.e. 'diffuse'), as indicated by the irregular/discontinuous ornament. White lines indicate Dauphiné twin boundary traces (note internal subgrain boundary traces, grey). Also shown are inferred grain boundary stress concentrations (triangles).

'diffuse'), as indicated by the irregular/discontinuous ornament in Figure 6. While many of these boundaries are broadly planar and at right angles to each other, there are some kinked boundary segments. Longer boundaries tend to occur centrally and define elongate 'subgrains' oriented transversally relative to the grain long axis. Most of the boundary traces at right angles occur towards the left periphery of the grain and define elongate subgrains subparallel to the grain long axis. However, towards the lower periphery of the grain, boundary orientations are more irregular and define smaller, somewhat equiaxed subgrains (Fig. 6).

(2) *Region B* is a rectangular region, larger and more distinct that the typical subgrains of region A but including similar subgrains and boundaries.

(3) *Region C* consists of several discrete irregular regions that penetrate from the grain periphery and appear to overprint and therefore at least post-date the initiation of the subgrain microstructures in the other regions. For identification, the boundaries are numbered and distinguished based on the region(s) their constituent subgrains inhabit (i.e. AA, AB, AC). The positions of grain boundary stress concentrations (e.g. owing to grain contacts – see Fig. 5), typically related to Dauphiné twinning (e.g. Lloyd 2000), are also indicated.

A composite key and example solution of plane-matching five-parameter boundary analysis is shown in Figure 7 and described below. For full details of this method, see Lloyd *et al.* (2021). The complete dataset for all boundaries analysed is provided in Supplementary Figure 1, with the detailed results listed in Supplementary Table 1. The Excel spreadsheet also provided enables solutions to the various crystallographic calculations involved in the five-parameter method. In each case, the local Euler angle triplets from either side of the boundary were obtained via EBSD. In general, the plane matching five-parameter boundary analyses provide the following information: (1) boundary plane and plane normal orientations in both crystallographic and stereographic coordinates; (2) boundary plane rotation angle/axis pair and tilt/twist angles; (3) boundary TTC value; and (4) the conventional EBSD disorientation angle/axis pair.

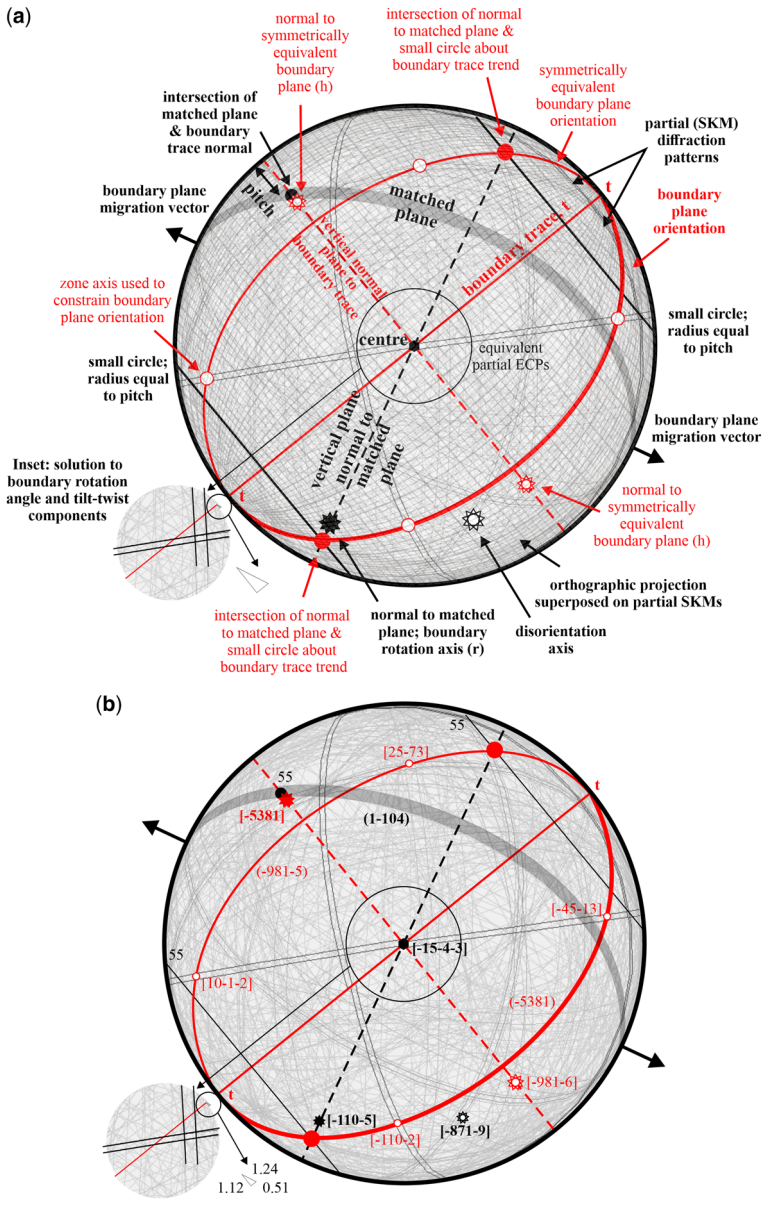

Fig. 7. Summary of plane matching boundary analysis. See Lloyd *et al.* (2021) for full details. (**a**) Key to ornamentation used throughout, based on boundary AA8. (**b**) Example of five-parameter boundary analysis for boundary AA8 (Fig. 6).

As an example solution for a typical plane matching five-parameter method analysis, consider subgrain boundary AA8 in Figure 6. The analysis for this boundary, based on the EBSD Euler angle triplets from either side (140.4, 112.2, 17.8 and 139.2, 112.7, 19.2 for a and b respectively), provides a single solution for the orientation of the boundary, as follows (Fig. 7b). Visual examination of the juxtaposition of the two partial SKMs across the common boundary trace reveals $(1\bar{1}04)$ to be the matched plane; its normal defines the boundary rotation axis (r) as parallel to $[1\bar{1}05]$. The matched plane intersects the normal to the boundary trace with a pitch of 55°, which defines the radius of the small circle about the

boundary trace (t). The intersections of the small circle with the vertical normal plane to the matched plane then constrain the great circle girdles that define the orientation of the boundary plane to two symmetrical possibilities: the stereographic orientations of these boundaries within the XYZ *upper* hemisphere projection are 051/48SE and 051/48NW. The equivalent crystallographic orientations of these planes are determined using SKMs to identify two zone axes in each girdle, which are substituted into the appropriate crystallographic equation (see Supplementary material Excel spreadsheet). The alternative solutions are parallel to $(\bar{9}81\bar{5})$ and $(\bar{5}\bar{3}81)$, with boundary normal directions (h) parallel to $[\bar{9}81\bar{6}]$ and $[\bar{5}\bar{3}81]$ respectively. Combined with the rotation axis of $[1\bar{1}05]$, the boundary normal directions yield TTC values of 0.67 and 0.04 respectively; the former indicates a general boundary, tending slightly towards twist, while the latter indicates close to a pure tilt boundary. The total boundary rotation angle about $[1\bar{1}05]$ determined from the partial SKMs is 1.24°, comprising a tilt component of 1.12° and a twist component of 0.51°. Consequently, as the boundary twist component is significant, the preferred boundary plane orientation is determined to be $(\bar{9}81\bar{5})$, which is close to $(\bar{1}100)$. Conventional EBSD disorientation analysis yields a single disorientation angle/axis pair for both boundaries of $3.5^\circ/\bar{8}71\bar{9}$, with the axis also being close to $(\bar{1}100)$. However, combing the disorientation axis with the relevant boundary plane normal direction yields different TTC values of 0.19 and 0.04 respectively. Both of these values indicate almost pure twist boundaries compatible with the non-preferred solution obtained via matched plane analysis.

It must be emphasized that not all boundaries yield a unique boundary plane orientation solution for several reasons, as follows.

(1) In most cases the reason concerns a definitive choice between the two symmetrical alternative boundary plane orientation solutions (Fig. 7). The ideal situation is when one of the alternatives is coincident with a low-index diffraction band in the SKM, although this appears to be rare and most potential solutions involve higher-index planes. Often, a choice can be constrained by considering the tilt (ω_{tilt}) and twist (ω_{twist}) components of the total rotation angle (ω) in terms of the angle between the boundary rotation axis (r) and the normal directions of the two planes. For example, if the angle is less than 45° then the alternative solution with the larger twist component is the most likely boundary and vice versa.

(2) Occasionally, a boundary may exhibit more than one matched plane (e.g. AA13, Supplementary Fig. 1), possibly owing to symmetry relationships or lack of clarity in the SKM fit. In such cases, the number of potential boundary orientation solutions is twice the number of matched planes. Fortunately, a discrimination is available in terms of the intersection of the small circle about the boundary trace and the vertical normal plane to the respective matched planes (see Fig. 7a). Usually, only one of the small circles intersects its plane normal and provides the single pair of symmetrical solutions, which can then be distinguished following the first approach.

(3) A configuration that does not comply fully with the plane matching method involves pure twist boundaries. For such boundaries the rotation axis is coincident with the boundary plane normal (i.e. TTC = 1.00) and consequently a matched plane cannot be defined (it is actually one of all lattice planes that are parallel to the boundary trace, t). However, the action of forming a pure twist boundary (i.e. where the tilt component is zero) results in all diffraction bands being displaced with not only the same sense but also the same magnitude; for example Supplementary Figure 1, boundaries AA7 and AA19 (dextral twist) and AA17 (sinistral twist).

AA boundaries. The complete set of results of the plane matching analyses are provided in Supplementary Table 1. The results are dominated by the AA boundaries, which are the most common in the grain (Fig. 6). As such, the statistical averages and standard deviations of the Euler angle triplets from each AA boundary ($139.6 \pm 2.8^\circ$, $113.6 \pm 1.9^\circ$ and $22.8 \pm 2.4^\circ$) can be used to define a general grain orientation, which is useful for comparison purposes. The small deviations are to be expected for these subgrains. Concomitantly, the average matched plane boundary misorientation angle is also small ($2.14 \pm 0.97^\circ$), as are the tilt ($1.26 \pm 1.00^\circ$) and twist ($1.43 \pm 0.92^\circ$) components. The equivalent average EBSD misorientation angle is compatible ($2.67 \pm 1.13^\circ$), although individual values can be more variable (see Supplementary Table 1 for details). In contrast, the average plane matching rotation and EBSD disorientation TTC values are significantly different at 0.59 ± 0.27 and 0.08 ± 0.06 respectively; the former suggests that intragranular boundaries are mostly general in nature, while the latter indicates that they are all close to tilt boundaries.

While it is useful to determine the average values of boundary rotations, disorientations and TTC, they do not provide a complete description. It is also necessary to consider the geometrical and crystallographic characteristics, which are best displayed graphically (Fig. 8, note composite key in Fig. 8a).

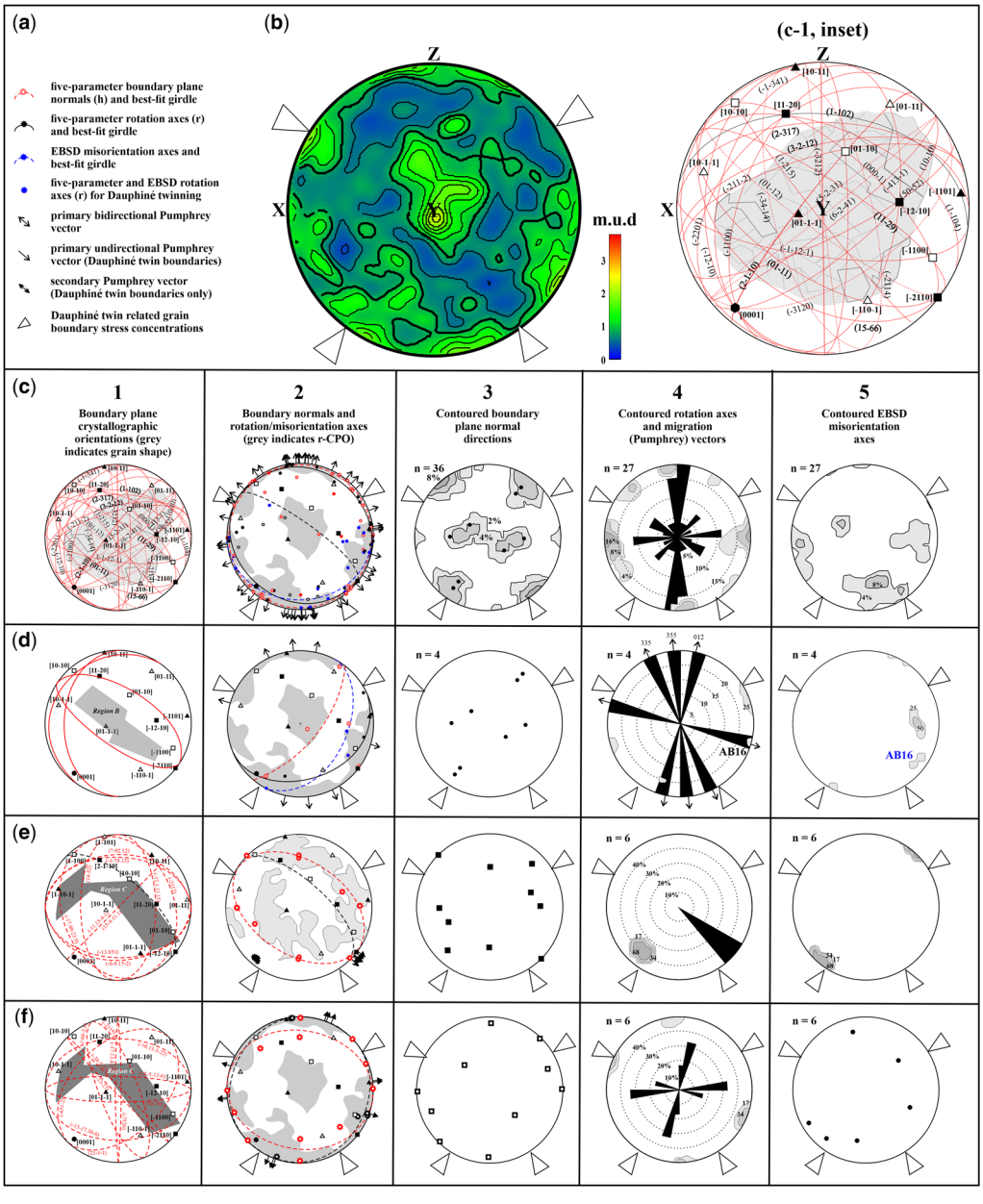

Fig. 8. Summary of boundary orientation analysis. (**a**) Composite key. (**b**) Positive rhomb *r*{10-11} CPO (contours multiples uniform distribution, m.u.d.); X (bedding dip direction), Y (bedding strike direction,) and Z (normal to bedding plane) bedding (017°/10°E) orientation reference frame applies to all projections. (**c**) AA subgrain boundaries; note detailed inset (C-1). (**d**) AB subgrain boundaries (too few data to contour). (**e**) AC subgrain boundaries; (000-1) matched plane. (**f**) AC subgrain boundaries; Dauphiné twin operation removed. In (**c**)–(**f**): 1, composite plot of subgrain boundary plane orientations (grey shadings, shapes of specific grain regions); 2, subgrain boundary plane normal directions and rotation/disorientation axes (grey shading, appropriate rhomb CPO); 3, subgrain boundary plane normal directions; 4, rotation axes and bi-directional boundary migration vectors; and 5, EBSD disorientation axes.

We first plot the positive rhomb CPO for the whole sample (Fig. 8b), which provides a useful indication of applied stresses and reflects grain boundary stress concentrations. Note that the equivalent positive rhomb positions for the individual grain are plotted in Figure 8c-1 (see inset for detail). The stereogram of AA subgrain boundary plane crystallographic orientations appears somewhat disorganized, even in the detailed inset (Fig. 8c-1). However, when expressed in terms of the equivalent boundary plane normal directions, definite patterns can be recognized (Fig. 8c-2). Boundary plane normal directions are either within the bedding (XY) plane or sub-parallel to stress concentrations (Fig. 8c-3). In addition (Fig. 8c-4), most boundaries exhibit bi-direction migration (Pumphrey) vectors parallel to Z (i.e. normal to bedding), although there is a minor trend sub-parallel to X (i.e. parallel to bedding dip). Concomitantly, most boundary rotation axes are oriented sub-parallel to X, usually sub-parallel to the XZ plane (Fig. 8c-4). In contrast, while most EBSD disorientation axes are oriented sub-parallel to either X or Z, they appear to be restricted to only half of the hemisphere of projection (Fig. 8c-5), which suggests the presence of some sort of symmetry operation, supporting the contention that disorientation and boundary orientation are not the same.

AB boundaries. In contrast to AA subgrain boundaries, there are relatively few AB subgrain boundaries (Fig. 6). The complete results for these boundaries are again provided in the Supplementary material. The statistical averages and standard deviations of the Euler angle triplets from the 'B-side' of AB boundaries are 133.8 $\pm$ 3.1°, 116.4 $\pm$ 2.3° and 19.8 $\pm$ 2.1° respectively, which are slightly different from the values for the 'A-side' (see above). As before, these values can be used to define a general grain orientation for region B. The average matched plane boundary rotation angle is approximately double that for AA boundaries at 4.96 $\pm$ 4.58°. Similarly, the tilt (3.94 $\pm$ 4.97°) and twist (2.35 $\pm$ 0.67°) components of these boundaries are also larger than the AA values. The equivalent average EBSD disorientation angle is somewhat larger (6.24 $\pm$ 1.87°) than the matched plane value. However, the AB dataset is influenced by boundary AB16 (see Fig. 6), which would be classed as effectively a grain boundary by both plane matching (i.e. rotation angle of 11.8°) and EBSD (disorientation angle of 9.1°) analyses. It is also almost a pure tilt boundary in terms of the matched plane (0.08) and EBSD (0.03) TTC values. As such, this boundary tends to skew the mean values of all parameters in the AB boundaries dataset; without it, the average rotation (tilt, twist) and disorientation angles are 2.68 $\pm$ 0.57° (1.46 $\pm$ 0.08°, 2.10 $\pm$ 0.54°) and 5.30 $\pm$ 0.78° respectively. The average plane matching rotation and EBSD disorientation TTC values are also different, at 0.51 $\pm$ 0.32 and 0.10 $\pm$ 0.07 respectively. The former is similar to the AA boundaries and suggests that AB subgrain boundaries are general in nature, while the latter is again indicating almost pure tilt boundary configurations.

As for AA-type boundaries, while it is useful to determine the average values of boundary rotations, disorientations and TTC, they do not provide a complete description of the geometrical and crystallographic characteristics of AB subgrain boundaries. These are best displayed graphically (Fig. 8d; see Fig. 8a for composite key). While there are few data, region B obviously has a similar positive rhomb $r\{10\bar{1}0\}$ pole figure CPO (Fig. 8d-1) to region A (Fig. 8c-1), reflecting grain boundary stress concentrations. AB boundaries therefore have boundary plane normal directions sub-parallel to stress concentrations (Fig. 8d-2, 8d-3; note the central orientations reflecting stress concentration subnormal to bedding). They also have similar migration bi-directions sub-parallel to Z, although more dispersed, while boundary rotation axes are somewhat dispersed relative to X but remain sub-parallel to the XZ plane (Fig. 8d-4). EBSD misorientation axes are typically oriented sub-parallel to X but again appear to be restricted to only half of the hemisphere of projection (Fig. 8d-5). As for AA boundaries, there is a clear difference between the matched plane rotation and EBSD disorientation axes. Combined together, these results suggest that the AB and AA boundaries have somewhat different characteristics.

AC (Dauphiné twin) boundaries. Region C penetrates into the grain from the grain boundary, usually from contacts with adjacent grains, and forms several isolated textural elements that share intragranular boundaries (i.e. AC) mainly with region A (Fig. 6). As for the other boundaries, the complete results for AC boundaries are provided in the Supplementary material. The statistical averages and standard deviations of the Euler angle triplets from the A side of the boundaries are 139.6 $\pm$ 1.9°, 113.6 $\pm$ 0.7° and 22.9 $\pm$ 3.5°, while for the C side of the boundaries they are 139.5 $\pm$ 2.1°, 113.4 $\pm$ 0.8° and 82.7 $\pm$ 3.6°. Thus, the values are effectively the same for both sides of the AC boundaries except for Euler 3, which is consistently *c.* 60° different and suggests that region C comprises Dauphiné twins. The twins are clearly visible in various EBSD maps (Figs 5 & 6) but not optically (Fig. 1d). However, while EBSD disorientation analysis consistently indicates a Dauphiné twin relationship of $\tilde{6}0°/[000\bar{1}]$ across AC boundaries (see the Supplementary material), there are problems with this interpretation. Dauphiné twins are penetration twins and

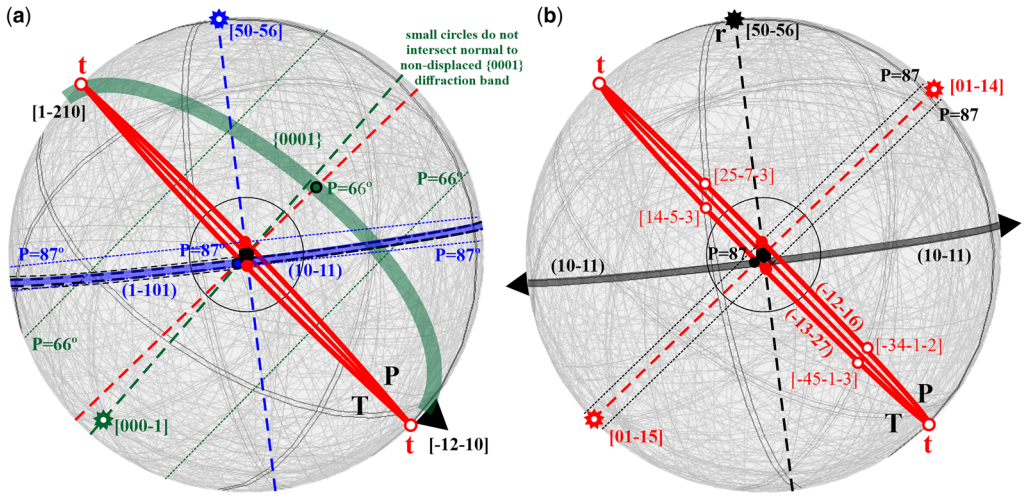

Fig. 9. Matched plane analysis of Dauphiné twin boundary AC1 (red symbols); orthographic projections. (**a**) Failed analysis (green symbols) based on Dauphiné twin law with $(000\bar{1})$ as the matched plane: small circles about trace, *t*, do not intersect normal to $(000\bar{1})$. Alternative solution (blue symbols) using 'family' $(1\bar{1}01)$ and $(10\bar{1}1)$ as matched planes. Note single twin boundary migration direction (black arrow) sub-parallel to boundary trace. (**b**) Revised alternative solution involving first removing Dauphiné twinning operation from Euler 3 and then recognizing $(10\bar{1}1)$ as the matched plane. Note double boundary migration directions (black arrows) at moderate angles to the boundary trace.

therefore the composition surface and twin plane are not coincident, leading to irregular twin boundaries (e.g. see Figs 5 & 6). Thus, EBSD disorientation analysis cannot define a specific AC boundary plane orientation as it always provides the same solution of $[000\bar{1}]$ for the disorientation axis (Fig. 8e-5), such that $(000\bar{1})$ should always be the boundary plane orientation, which is clearly not possible. Although matched plane analysis should provide a solution, it is not as straightforward as the equivalent situation for subgrain (i.e. AA or AB) boundaries.

Matched plane analysis of Dauphiné twin (AC) boundaries

As Dauphiné twinning involves 60° rotation about the *c*-axis, this suggests that the matched plane for all Dauphiné twin boundaries is {0001}. Unfortunately, this plane is too broad to be visible in EBSD patterns, although it can be defined by constructing a great circle through the three $a\langle 11\bar{2}0\rangle$ axes. However, as the traces of Dauphiné twins are typically highly irregular (e.g. Figs 5 & 6), their boundary segments must have different orientations, which suggests that they should also have different matched planes. In general, the Dauphiné twin angle/axis pair relationship of 60°/<0001> (i.e. $\theta/\langle uvwt\rangle_L$) restores the parent lattice configuration of the twin. This is not necessarily the same as the boundary rotation angle/axis pair (i.e. ω/r or $\omega/\langle uvwt\rangle_B$), especially for penetration twinning, as indicated by the observed variations in twin boundary traces. In fact, the assumption that {0001} is the matched plane *forces* the analysis to comply with the constraints imposed by EBSD disorientation analysis and sometimes results in there appearing to be no boundary plane solution. This usually occurs because the small circle about the strike of the trace, as defined by the pitch of the intersection between the matched plane and the normal to the trace, does not intersect the normal to the matched plane (see Fig. 7a for details). An example is shown in Figure 9a for boundary AC1. Thus, use of the disorientation axis to define the matched plane is not justified.

For Dauphiné twin boundaries, a matched plane can usually be recognized if family relationships are considered. For example, examination of the diffraction relationships across the boundary in Figure 9a recognizes that the parent $(10\bar{1}1)$ and twin $(1\bar{1}01)$ diffraction bands are matched, although they represent opposite rhomb forms; the former is characterized by only first-order diffraction, while the latter exhibits first- and second-order diffraction. This configuration defines $\{10\bar{1}1\}$ as a matched plane and its normal therefore constrains the boundary rotation axis to $\langle 50\bar{5}6\rangle$. The intersection of the matched plane with the boundary trace normal defines a pitch and hence small circle angles of

87°, which intersect the normal to the matched plane to define symmetrical sub-vertical boundary planes (Fig. 9a). Although providing a potential solution, this approach depends on the validity of using families of, rather than identical, matched planes, which may not be crystallographically rigorous and requires further justification.

EBSD disorientation analysis of Dauphiné twin boundaries does not usually define the angle to be precisely 60°; differences of a few degrees are not uncommon (see the Supplementary material). Such behaviour can be explained by 'relaxation models' for allowable deviations ($\Delta\theta_{max}$) from exact CSL boundary configurations that could be sustained by a dislocation array (e.g. Brandon 1966). While several 'relaxation criteria' exist (e.g. Brandon 1966; Ishida and McLean 1973; Pumphrey 1976; Palumbo *et al.* 1998), they are all of the form (e.g. King and Shekhar 2006),

$$\Delta\theta_{max} = \theta_0\Sigma^{-n}; 1 \leq \Sigma \leq \Sigma_{max} \qquad (5)$$

where $\theta_0 = 15°$ (although perhaps this should be 10° for minerals), n varies from 0.5 (least restrictive) to 1 (most restrictive) depending on criterion and Σ is the ratio of the primitive CSL unit cell volume to the primitive crystal unit cell volume, often expressed as the fraction of coincident atoms shared by the domains on either side of a boundary; significant Σ-values range from 1 (low-angle grain boundaries) to usually 25. While application of relaxation criteria can explain the deviation of Dauphiné twin misorientation angles from the ideal value of 60°, there is another intriguing possibility that also provides a solution to boundary orientation determination via matched plane analysis.

Using Figure 9a, if $(000\bar{1})$ is considered to be the matched plane, then the boundary migration direction is constrained to be parallel to either $(1\bar{2}10)$ or $(\bar{1}2\bar{1}0)$. However, as the twin is penetrating into the parent grain from the periphery (see Fig. 6), migration must be parallel to the penetration direction. Boundary migration is therefore unidirectional for all AC boundaries considered (Fig. 8e-4), which implies that migration cannot occur in other directions. Such restraint suggests that Dauphiné twins cannot 'spread' laterally compared with their 'penetration' direction. Nevertheless, the observed twin microstructures (Fig. 6) do appear to indicate both penetration parallel and also lateral boundary migration. The latter can be explained if the boundary orientation and migration direction are defined by the alternative matched plane 'family' diffraction band (Fig. 9a). Unfortunately, this construction has its problems, specifically, the fact that the boundary juxtaposes lattices mismatched by 60° and crystal planes/directions on one side of the boundary relating to directions/planes on the other side, leading to problems with indexing. Recalling that the Dauphiné twin EBSD disorientation angles differ slightly from the ideal value, it is possible that the deviations, rather than being due to relaxation criteria, actually reflect the subsequent modification of initially ideal twin boundaries by non-twin related (i.e. 'subgrain') boundary migration. This hypothesis can be tested by removing the twinning operation, as follows (Fig. 9b).

The Dauphiné twinning operation can be removed by simply adding/subtracting 60° from the third Euler angle for the twinned region so that its value becomes similar to that of the parent region. Thus, for the example shown in Figure 9a, the parent Euler angle triplet is (140.3°, 114.1°, 22.8°) and so the twin triplet of (139.5°, 113.1°, 82.0°) becomes (139.5°, 113.1°, 22.0°). Ideally, the two domains should have identical Euler Angles triplets (i.e. the original parent orientation of the twin domain has been restored) but this is not the case and the triplets are slightly different. The two domains can be construed to be separated by an intragranular subgrain boundary, which can be fully analysed by the conventional plane matching method (Fig. 9b). A similar approach has been applied to the other AC Dauphiné twin boundaries and the composite set of results for these boundaries can be presented and compared (see the Supplementary material). The statistical averages and standard deviations of the Euler angle triplets from the A, C and modified-C sides of the boundaries are now (139.1 $\pm$ 1.8°, 113.8 $\pm$ 0.4°, 21.9 $\pm$ 2.8°), (138.8 $\pm$ 1.5°, 113.7 $\pm$ 0.5°, 81.7 $\pm$ 2.9°) and (138.8 $\pm$ 1.5°, 113.7 $\pm$ 0.5°, 21.7 $\pm$ 2.9°), respectively. These values are effectively the same for both sides of the AC boundaries, confirming that region C developed from region A by Dauphiné twinning.

AC (Dauphiné twin) boundaries:composite results

Unsurprisingly, the average EBSD disorientation (59.7 $\pm$ 0.1°) is close to the ideal value for Dauphiné twinning. In contrast, assuming $(000\bar{1})$ as the matched plane, the average value (54.3 $\pm$ 2.3°) for the plane matching method is sufficiently different from the ideal that the boundaries would be considered to be not Dauphiné twins but HAGBs. This discrepancy almost certainly arises from constraining the matched plane to $(000\bar{1})$ and hence the misorientation axis to $[000\bar{1}]$ irrespective of the twin boundary plane orientation. Nevertheless, it is possible to determine potential boundary plane orientations (see Supplementary material) and hence TTC values for each boundary according to the two methods. For EBSD, the average TTC value is 0.08 $\pm$ 0.06, while for plane matching it is 0.43 $\pm$ 0.34. Thus, EBSD

disorientation analysis recognizes all Dauphiné twins as essentially pure tilt boundaries, whereas plane matching considers them to be general boundaries, although the standard deviation is such that boundary type extends from effectively pure tilt to almost pure twist. The matched plane interpretation is consistent with the variable range in twin boundary trace orientations observed in the microstructural maps, whereas the disorientation is not.

Removing the Dauphiné twin operation defines the AC boundaries as subgrain boundaries with an average plane matched rotation angle of $1.1 \pm 0.6°$, with average tilt and twist components of $0.9 \pm 0.4°$ and $0.6 \pm 0.5°$ respectively and average TTC of 0.49 ± 0.17. The latter suggests that the AC 'subgrain' boundaries are general with almost equal tilt and twist components. In comparison, the equivalent average EBSD disorientation angle is $0.9 \pm 0.5°$, while its average TTC is 0.10 ± 0.04, which suggests that the AC 'subgrain' boundaries have essentially pure tilt configurations.

Again, while it is useful to determine the average values of boundary rotations, disorientations and TTC, they do not provide a complete description of the geometrical and crystallographic characteristics of AC boundaries. These are best displayed graphically (Fig. 8e, f; see Fig. 8a for the composite key). Owing to Dauphiné twinning, region C has the opposite rhomb pole figure CPO (Fig. 8e-1) compared with the rest of the grain as the *r* and *z* directions are interchanged (e.g. Fig. 8c-1); nevertheless, it still reflects grain boundary stress concentrations. The stereogram of AC matched plane boundary crystallographic orientations conforms in part to the shape of region C1 (Fig. 6), although it is not possible to distinguish the symmetrically equivalent solutions (Fig. 8e-1). However, if the Dauphiné twin operation is removed, the predicted matched plane AC 'subgrain' boundary orientations replicate the shape of region C1 (Fig. 8f-1). In terms of the equivalent boundary plane normal directions, Dauphiné twin matched plane normals define moderately dipping symmetrical great circles somewhat consistent with the *z*-rhomb sample CPO, while EBSD disorientation axes define a single twin boundary plane (Fig. 8e-2, 3). Both approaches indicate unidirectional boundary migration vectors parallel to the axis of the twinned region and also the $[\bar{1}2\bar{1}0]$ crystal axis (Fig. 8-e-1, 2 & 4), consistent with the twin penetration direction observed in the grain microstructure (Fig. 6). Removing the twinning operation also results in both matched plane and EBSD disorientation boundary normals defining symmetrical but different great circles that dip shallowly sub-parallel to XZ and the sample *r*-rhomb CPO (Fig. 8f-2, 3). In addition, boundary migration vectors are not only bidirectional but also indicate lateral migration directions (Fig. 8f-2, 4). In contrast to the approximately constant EBSD disorientation axes orientation for Dauphiné twinning (Fig. 8e-5), the same axes are dispersed if the twinning operation is removed (Fig. 8f-5).

Discussion

While the principal aim of this contribution is to show how microstructures can be mapped in detail on the scale of individual grains up to the thin section, nevertheless perhaps the most important result is that conventional EBSD-based misorientation analysis cannot usually distinguish either boundary type or mis/dis-orientation based on Euler angle triplets alone. Indeed, such EBSD analysis may be seriously misleading as it considers all boundaries to have near-tilt configurations. Cross and Randle (2003) have shown that the lowest-angle disorientation distribution alone provides an incomplete and ambiguous description of boundary plane configurations. Using the complete five parameter definition of boundaries, Kim *et al.* (2005) recognized a preference for (asymmetrical) hi-tilt and hi-twist boundary types in grain boundary engineered alpha brass. In general, studies on metals and ceramics suggest that the grain boundary plane, rather than the misorientation, is the key parameter when defining boundaries (e.g. Pennock *et al.* 2009). The matched plane method used in this contribution offers the potential to determine boundary plane types, orientations and rotations in both crystallographic and physical (e.g. sample kinematic) frameworks, from which a wide range of microstructural maps can be produced. The results of this contribution are now discussed in terms of their general implications and also how they can contribute to microstructural mapping.

Interpretation of results

Perhaps the most immediate impression of the results of boundary orientation determination presented above is that there are apparently many solutions that often appear incompatible. How then can an accurate microstructural map of subgrain boundary orientations be constructed? It is first necessary to understand why there is such a range of potential solutions.

The analyses presented not only involve two distinctly different approaches, matched plane and (EBSD) disorientation, but they also yield fundamentally different results. The former attempts to define the orientation of the boundary plane, whereas the latter recognizes the disorientation between the crystal lattices on each side of a boundary (see Fig. 2). In general, these are not the same, although in specific situations they may be (see Fig. 8e, f). For example, adjacent pairs of sedimentary grains shown in

Figure 5a can all be described in terms of an (EBSD) disorientation angle/axis pair that rotates the adjacent crystal lattices into parallelism. However, this is independent of the orientation of the physical boundary that separates each pair, which depends on sedimentological processes (e.g. erosional, grain shape and depositional conditions). Similarly, in terms of subgrain boundaries, the TTC angle/axis pair is a rotation about an axis relative to the boundary plane, not a crystal lattice (Fig. 2). While there is always a common crystallographic axis across a boundary, this does not usually define the boundary plane orientation. Indeed, while disorientation analysis determines the smallest angle/axis pair required to bring adjacent crystal lattices into parallelism, the actual boundary plane can have a wide range of physical orientations, with concomitant critical implications for boundary characteristics and behaviour. Thus, the different results obtained by the matched plane and (EBSD) misorientation analyses are to be expected and are not contradictory; they are simply describing different properties.

Another explanation for the range of boundary orientation solutions obtained relates to the reference frame of the solutions. This is specifically associated with the matched plane method. All boundary plane orientations can be considered in terms of either the crystallographic reference frame or a physical reference frame (Fig. 8c–f); geologically, the latter are usually geographical (i.e. north, south, east, west) and/or kinematic (i.e. $X \geq Y \geq Z$, although not the same XYZ as used in this contribution, which relate to bedding). Thus, the different solutions simply reflect the different reference frames available. The particular reference frame chosen depends on the specific relationship investigated (e.g. preferred crystallographic orientation of boundary planes, relationship between boundary orientation and deformation kinematics).

The results shown in Figure 8e and f are not maps per se; rather, they are types of projections (specifically orthographic/gnomonic to comply with the SKMs). Figure 10 illustrates some of the microstructural (grain) maps that can be produced via the approach described in this contribution. The first map (Fig. 10a) shows the standard EBSD defined boundary arrays for specific disorientation angles (indicated in the key) and forms a 'base map' that clearly outlines the individual subgrains and twins. The second map (Fig. 10b) plots the matched plane boundary rotation angles and associated TTC values, including consideration of the Dauphiné twin boundaries both with and without the twin operation (insets). Most rotation angles are small ($<5°$) and most boundaries are general, although several pure tilt or pure twist boundaries are present. The twin boundaries have rotation angles almost 10° smaller than the ideal but without the twin operation the rotation angles are similar to most of the other subgrain boundaries. Thus, the twin misorientation axis does not constrain the boundary orientation, which is defined by subtracting the twin operation. The third map (Fig. 10c) treats the boundaries as though they are faults and plots their physical orientation in terms of strike/dip/sense, including considering the Dauphiné twin boundaries both with and without the twin operation (insets). Dips are extremely variable, ranging from *c.* 10° to vertical, although some senses are indeterminate, including the twin boundaries, which also have different dips with and without the twin operation. Treating the boundaries akin to faults also allows 'cross-sections' to be constructed and hence the prediction of grain shape beneath/above the analytical surface (Fig. 10c). The fourth map (Fig. 10d) plots the boundary migration vectors. In most cases these are bi-directional and therefore provide two opposite migration senses. Nevertheless, they do provide constraint on potential boundary movement kinematics and hence subgrain evolution. Migration senses are unidirectional for the twin boundaries, assuming that the twinned regions are penetrating into the grain from grain boundary stress concentrations. As such, the migration vector has a constant direction for all twin boundaries irrespective of their orientation (trace) if the twin operation is included. However, removing the twin operation indicates migration directions at high angles to the boundary traces, which allows the twins to spread laterally relative to the propagation (penetration) direction. Many other types of microstructural maps are also easily achieved with current and developing software facilities.

Dauphiné twinning

Both the sample considered in this contribution and the individual grain mapped in detail exhibit significant Dauphiné twinning as well as subgrains (Figs 5 & 6). As previously stated, the presence of Dauphiné twinning introduces a consistent intragranular misorientation of 60°/<0001>. However, while the lattice misorientations associated with Dauphiné twinning remain consistent for all examples, the typical irregularity of Dauphiné twins means that their complete boundary orientations must vary (e.g. Figs 8–10). Thus, it is not expected that EBSD disorientation solutions for Dauphiné twin boundaries should be consistent with matched plane solutions. It seems appropriate therefore to consider in some detail the implications and significance of mapping Dauphiné twinning in quartz rocks.

Dauphiné twinning is an example of 'twinning without change of form' (Klassen-Neklyudova 1964) and involves only atom shifts, which are small relative to interatomic separations, rather

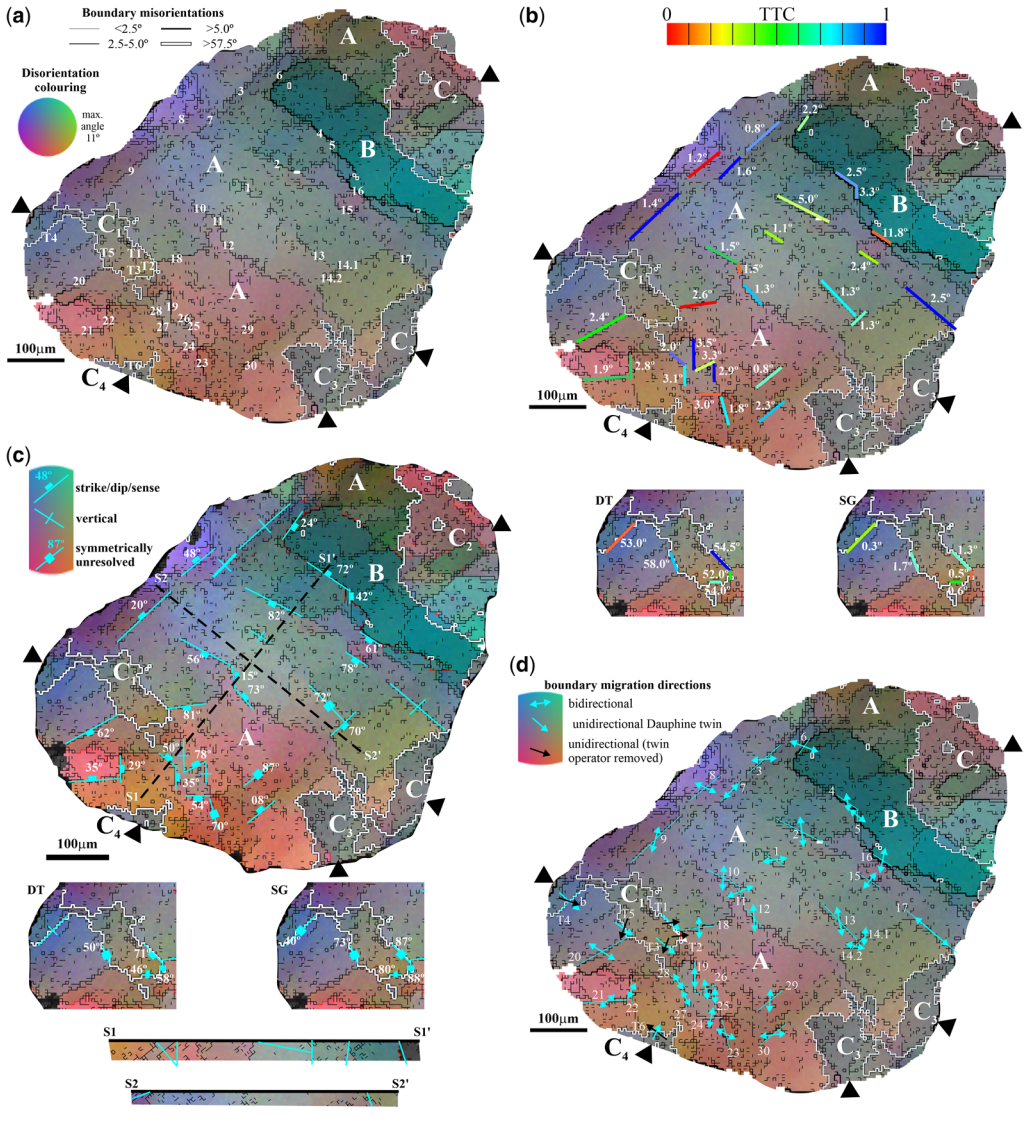

Fig. 10. Grain microstructure maps. (**a**) EBSD boundary misorientation angles. (**b**) Matched plane boundary rotation angles and TTC values; insets, with (DT) and without (SG) Dauphiné twin operation. (**c**) Boundary strike/dips/senses; insets, with (DT) and without (SG) Dauphiné twin operation. Note also cross-sections S1–S1′ and S2–S2′. (**d**) Boundary plane migration vectors.

than twin gliding owing to shear. Thus, Dauphiné twinning is displacive and not reconstructive. Dauphiné twins form under the application of concentrated loads on various faces of twin-free grains (see Klassen-Neklyudova 1964, especially for a review of early, non-English, work) and twin interfaces subsequently move under effective stresses (e.g. Thomas and Wooster 1951; Aizu 1973; Newnham *et al.* 1975), for example, *c.* 500 MPa at room temperature and *c.* 1–10 MPa at 400–500°C. Dauphiné twin interfaces are ideally planar (Aizu 1970; Newnham and Cross 1974), but easily adopt arbitrary configurations (e.g. Figs 5 & 6). It has been suggested therefore (e.g. Cahn 1978) that it is helpful to regard Dauphiné twin boundaries as grain boundaries involving two fixed orientations; this may be similar to the approach described above involving removal of the twin operation, in which case the twin boundaries are considered as subgrain boundaries. While Dauphiné twins do not develop via shear, they do develop under applied stresses. However, as their boundaries continue to migrate in the same

direction if the stresses are reversed, this suggests that stored elastic energy, which involves the square of the applied stresses, is significant (Thomas and Wooster 1951). Thus, the twins continue to grow and/or contract in such a way that the net result is the whole grain yields as much as possible under a given applied stress (e.g. Cahn 1978). Although this behaviour has been widely verified both experimentally and theoretically for applied stress (see review in Paterson 1973), it is not valid for applied strain (e.g. Tullis and Tullis 1972). Thomas and Wooster (1951) coined the phrase piezocrescence to explain the behaviour of quartz under applied stress.

Tullis and Tullis (1972) showed that more compliant directions (i.e. sub-parallel to $r\langle 10\bar{1}1\rangle$) tended to align with the applied stress (Fig. 11a), resulting in strong *r*-maxima CPO owing to Dauphiné twinning, in contrast to a deformation texture, which would produce an approximate c[0001] parallel stress axes maximum. Combinations of Dauphiné twinning and deformation therefore result in texture maxima between $r\{10\bar{1}1\}$ and *c*[0001] depending on the individual contributions. The effect of Dauphiné twinning is most noticeable where there are only small permanent (i.e. crystal plastic) strains but persists up to strains of 30–50%. It is exacerbated with increasing temperatures up to a limiting temperature beyond which no further strengthening occurs (Tullis and Tullis 1972). The limiting temperature is lower for purer quartzites, while finer grained samples formed stronger Dauphiné twin-related textures than coarse-grained samples. Tullis and Tullis (1972) further observed that while for small strains

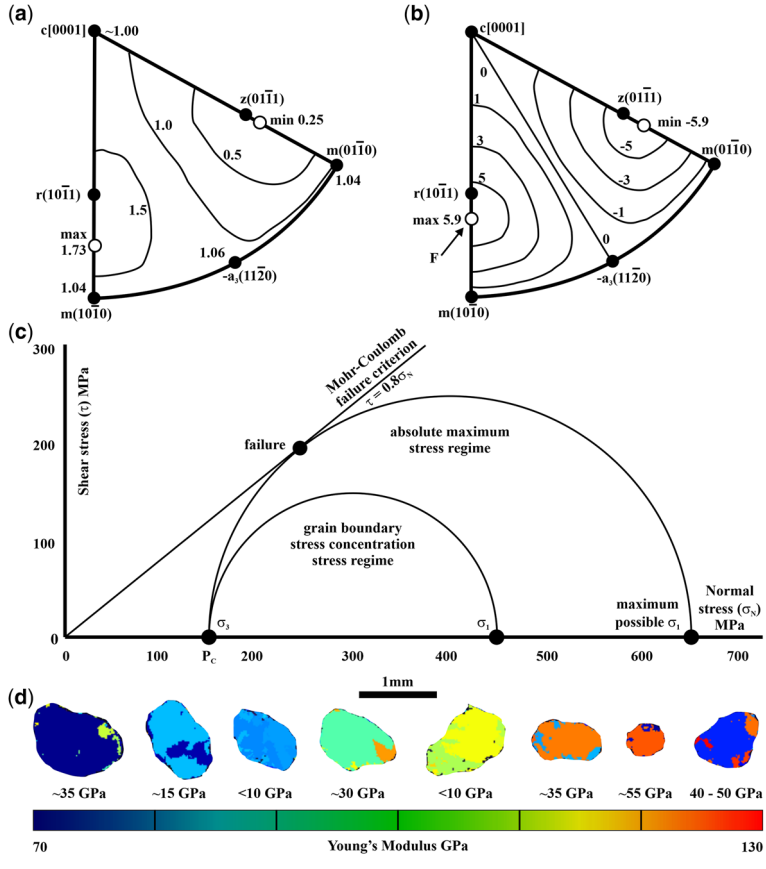

Fig. 11. Dauphiné twin-texturing. (**a**) Inverse pole figure distribution of stress axis (contours, multiples of uniform distribution) relative to quartz unit cell in flint loaded to a differential compressive stress of 1.3 GPa at 500°C and 400 MPa confining pressure for 3 h. (**b**) Inverse pole figure variation with crystal direction in quartz of difference in elastic compliance ($\Delta S'_{11}$) between parent and twin orientations; units are 10^{-6} 1 MPa^{-1}; F, most favourable oriented grain. Both figures modified in terms of units from Tullis (1970) and Tullis and Tullis (1972). (**c**) Mohr circle construction based on sample location defining potential differential stresses to which the selected sample could have been subjected. (**d**) Examples of Young's modulus variations in Dauphiné twinned grains.

and constant temperature and purity, increasing the applied stress strengthened the Dauphiné texture, large increases in stress were needed to achieve only modest increases in texture, which suggests that texture intensity is not proportional to the driving force to move a Dauphiné twin boundary (see below). Finally, in their experiments, Tullis and Tullis (1972) observed that while some samples deformed to substantial plastic strains underwent dynamic recrystallization, others did not but a strong Dauphiné texture developed in both cases. This suggests that Dauphiné twinning patterns are repeatedly formed after successive phases of recrystallization.

The experimental observations of Tullis and Tullis (1972) indicate that where Dauphiné twinning obeys the elastic strain energy criterion, it exerts a significant control on texture development in deformed quartz rocks even when permanent plastic strain is absent. However, very many subsequent studies indicate that intense plastic deformation (e.g. quartz mylonites) induces *c*-axis textures that are strong enough to swamp the Dauphiné twinning driving forces. Nevertheless, the description of the impact of Dauphiné twinning on texture and CPO evolution is clearly applicable to the sample and individual grain considered in this contribution (Figs 5 & 6). All of the observed boundaries are assumed to have developed under diagenetic, non-metamorphic conditions without obvious deformation. The sample therefore exhibits the expected distinct *r*-rhomb CPO (Fig. 5c), consistent with quartz single crystal Young's modulus behaviour in which maxima and minima are related to the $r\{10\bar{1}1\}$ positive and $z\{0\bar{1}11\}$ negative rhombs respectively (Fig. 5d). For example, the central (i.e. Y-parallel) and diffuse peripheral (i.e. XZ-parallel) $r\{10\bar{1}1\}$ maxima reflect minima in Young's modulus and are also consistent with grain boundary contact stress concentrations (e.g. Gallagher *et al.* 1974; Lloyd 2000). More general contact stresses are responsible for the development of subtle and diffuse subgrain microstructures indicative of low-temperature plasticity (e.g. Lloyd and Knipe 1992).

It is possible to estimate the driving force (ΔW) required to move Dauphiné twin boundaries, assuming uniaxial compression under hydrostatic conditions (e.g. Eshelby 1970; see Cahn 1978),

$$\Delta W = 0.5\Delta S'_{11}\sigma^2_{1-3} \qquad (6)$$

where σ_{1-3} is the differential (compressive) stress, S'_{11} is the reciprocal of Young's modulus (i.e. the elastic compliance) in the direction of the applied stress and $\Delta S'_{11}$ is the difference in S'_{11} between the two constituent orientations of the Dauphiné twin. Thus, ΔW measures the elastic energy in a grain consisting entirely of one or other of the twin orientations (Tullis and Tullis 1972). However, in more complex stress systems a tensoral approach is more appropriate (Newnham 1975; Anderson *et al.* 1976). To estimate the driving force for Dauphiné twin-texturing via the elastic strain energy criterion, Cahn (1978) used the experimental data of Tullis (1970) and Tullis and Tullis (1972); the specific experiment showed that a substantial permanent strain is produced over several hours at *c.* 500°C by a differential uniaxial stress of *c.* 1500 MPa. Following Cahn (1978) but adopting modern units, the value of $\Delta S'_{11}$ is defined by the most favourably orientated grain, which is sub-parallel to $r\{10\bar{1}1\}$ (Fig. 11a) and from Figure 11b is 5.9×10^{-6} 1 MPa^{-1}. From equation (6), the driving force is therefore 6.6 MPa, or in terms of gram molecular mass *c.* 172 J mol^{-1}. Such a large driving force is due to the high differential stress needed for quartz to deform plastically, even at 500°C (e.g. Doukhan and Trepied 1985; Muto *et al.* 2011). While data for stored energy of plastic deformation in quartzite are lacking, Cahn (1978) argued that as values for metals deformed to strains significantly greater than those in the quartzite experiments are typically much lower than the calculated driving force for Dauphiné twinning, it suggests that the driving force for Dauphiné twinning is somewhat greater than that for conventional recrystallization of plastically deformed quartz rock. If this comparison is valid, it explains why strong Dauphiné twinning textures can form not only in undeformed sedimentary rocks (e.g. Fig. 5) but also in permanently deformed and recrystallized quartzites.

In terms of the grain selected for detailed analysis, it exhibits several distinct twinned regions (Fig. 6). Rather than use Figure 11b, which relies on in the direction of the applied stress, the Young's modulus map of the grain (Fig. 5e) is preferred to provide values of $\Delta S'_{11}$. The map indicates that the twins (i.e. regions C) have values ranging from 120 to 130 GPa, while the value for the grain (i.e. regions A and B) is effectively constant at *c.* 80 GPa. The differences between these values (i.e. 40–50 GPa) therefore define the range of $\Delta S'_{11}$ as $4–5 \times 10^{-4}$ 1 MPa^{-1}. However, determining the driving force (s) for twinning in the grain via equation (6) also requires knowledge of the differential stress, which can only be estimated from the geological conditions of the sample location. Assuming a maximum depth of burial of *c.* 6 km, the confining pressure (P_c) is *c.* 160 MPa (using a density of 2700 kg m^{-3}). As the sample location lies just outside the deformation zone of the Skiag Bridge back thrust, this is potentially the value of a homogeneous hydrostatic stress system (i.e. all principal stresses equal). However, this would mean that the differential stress is zero and hence there is no driving force for twinning.

For a differential stress to exist requires an inhomogeneous hydrostatic stress system. An absolute maximum possible principal stress (σ_1) occurs as the rock is about to fracture, although there is no evidence for this in the sample (see Fig. 5a). Nevertheless, it provides an upper limit and can be estimated via Mohr Circle construction by adopting a conventional Mohr–Coulomb fracture criterion (Fig. 11c). As the sample is located within the immediate foreland to the Moine Thrust Zone, a short distance from the Skiag Bridge backthrust, the applied stress regime is likely to have involved subhorizontal compression. Assuming that the stress system is Andersonian, the minimum (σ_3) principal stress is subvertical and equal to the confining pressure, which constrains the absolute maximum principal stress at fracture to be *c.* 650 MPa, resulting in a maximum differential stress of *c.* 500 MPa.

The actual differential stresses in the sample will have been lower than the predicted value at fracture as no fractures are observed in the sample. As the absolute minimum principal stress value is constrained by the confining pressure, the maximum principal stress values must have been greater than *c.* 150 MPa. In addition, they are likely to have been increased owing to local stress concentration effects at grain contacts (see Figs 5 & 6). Unfortunately, magnitudes of stress concentrations are generally unknown, although very large stress concentrations can occur at crack tips. Photo-elastic experiments (Berka 1982) provide some guide and suggest that magnitudes may be up to three times the predicted normal stress, with the magnitude of the concentration depending on the orientation of the contact boundary relative to the principal stresses. For the purpose of this analysis, a stress concentration of 450 MPa (i.e. three times the minimum principal stress) has been adopted, resulting in a differential stress of 300 MPa (Fig. 11c).

The potential driving forces for Dauphiné twinning in the selected grain can be estimated by substituting the relevant values into equation (6), including the estimated range of $\Delta S'_{11}$. For the maximum conditions at fracture they are calculated to be 3.13–2.50 MPa or 81–65 J mol^{-1}, while for the values owing to grain boundary stress concentrations they are calculated to be 1.1–0.9 MPa or 29–23 J mol^{-1}. These values are significantly less than the experimental values owing to the much lower differential stresses involved but still larger than the values of the stored energy of plastic deformation in metals (Cahn 1978), even though the sample is essentially undeformed.

As it is possible to map the variation in Young's modulus for the whole sample via EBSD data (e.g. Fig. 5e), it is consequently also possible to map the values of the driving forces for Dauphiné twinning from grain to grain. Although producing such a map is beyond the scope of this contribution, a cursory examination of the Dauphiné twinning textures in terms of the differences in Young's modulus between parent and twin produces some interesting observations. Figure 11d shows a number of grains with Dauphiné twins from the sample, including the selected grain for reference. The differences in Young's modulus between parent and twin regions are significant and range from $<$10 GPa to *c.* 55 GPa depending on their relative crystal orientations. Assuming as before a constant (maximum) differential stress owing to grain boundary stress concentrations of 300 MPa, the driving forces for twinning range from *c.* 0.8 to *c.* 7 MPa or from *c.* 21 to *c.* 182 J mol^{-1}. It seems therefore that the differences in Young's modulus between parent and twin and hence the driving forces for twinning do not need to be large, which explains the propensity for Dauphiné twinning in diagenetic and low-grade metamorphic quartz and its favourable competition with dynamic recrystallization as a texture forming process. Microstructural maps of such rocks and textures should reflect this competition and prove useful in the investigation of microstructural evolution.

Boundary plane properties

It is well known that many polycrystalline material properties, characteristics and behaviours are affected by the nature of intra/inter-granular boundaries (e.g. Sutton and Balluffi 1995; Langdon 2006; De Graef and McHenry 2012). The matched plane method used in this contribution allows the complete orientation of boundary planes to be determined. It therefore has the potential to critically impact further understanding of these properties, characteristics and behaviours in a microstructural mapping framework. In particular, it should help to constrain and/or explain boundary behaviour, which may then become a mappable property at the microstructural scale. Boundary properties of immediate interest are mobility, energy and excess volume. While the first has been considered in relation to Dauphiné twinning, detailed investigations of these and other properties are beyond the scope of this contribution. Nevertheless, such investigations are now possible given the ability to determine and map the complete orientation of boundaries in polycrystalline samples via the matched plane method.

Conclusions

The continued development of advanced analytical techniques such as EBSD has today made the mapping of geological microstructures on the subgrain to thin-section (and potentially larger) scales commonplace. While most investigations continue to

relate microstructures and textures via the determination of CPO, focusing on grains and subgrains, there is developing interest in other microstructural elements, such as the boundaries that separate these regions. This contribution applies a recently developed method, here termed matched plane, that provides the full five-parameter definition of boundary plane orientation in terms of boundary plane rotation angle/axis and boundary plane normal angle/azimuth. The method is used to analyse the orientations of boundaries in an undeformed sedimentary quartzite, focusing on an individual representative grain to construct various microstructural maps. Most subgrain boundaries have general configurations with misorientations of only a few degrees, plane normal directions sub-parallel to the quartz crystal $r\langle 10\bar{1}1\rangle$ direction and rotation axes sub-parallel to bedding, with migration directions parallel to bedding normal. In contrast, conventional EBSD disorientation analysis indicates that most subgrain boundaries are close to pure tilt configurations, with axes oriented sub-parallel to either bedding dip or normal. Matched plane and EBSD disorientation analyses are therefore fundamentally different; the former determines boundary type, rotation and orientation, while the latter only determines the angle/axis rotation require to bring adjacent crystal lattices into parallelism.

In addition to subgrains, Dauphiné twins are clearly visible in the EBSD-based maps. While EBSD disorientation analysis of twin boundaries indicates tilt configurations with angles/axes consistently close to 60°/[0001], matched plane analysis yields somewhat lower boundary plane rotation angles with boundary configurations ranging from tilt to twist. However, the variable traces of Dauphiné twin boundaries means that their boundary plane orientations must also vary. Although EBSD disorientation analysis cannot distinguish this variation, it is recognized by removing the twinning operation from the matched plane analysis. The results indicate that twin boundary planes comprise effectively equal tilt and twist components, are oriented sub-parallel to $r\langle 10\bar{1}1\rangle$ within the bedding plane and can migrate both parallel and laterally relative to the twin penetration direction. In addition, the driving force for twin boundary migration is determined as *c.* 0.8–7 MPa (*c.* 21–182 J mol^{-1}) by mapping differences in Young's Modulus between parent and twin ($<$10 to *c.* 55 GPa,) and estimating the local differential stress (*c.* 300 MPa). Such low values explain the propensity for Dauphiné twinning in diagenetic and low-grade metamorphic quartz and suggest that twinning could compete favourably with dynamic recrystallization as a texture forming process.

Acknowledgements I thank Amicia Lee and Maren Kahl for their help in developing the matched plane method. I also thank Betty Mariani, an anonymous reviewer and the special editor, Rob Butler, for their comments, which have helped improve the final version. The sample used in this contribution was collected by GEL and Rob Knipe as part of UK NERC grant GR3/4461 at the University of Leeds.

Competing interests The authors declare that they have no known competing financial interests or personal relationships that could have appeared to influence the work reported in this paper.

Author contributions **GEL**: conceptualization (lead), data curation (lead), formal analysis (lead), funding acquisition (lead), investigation (lead), methodology (lead), project administration (lead), resources (lead), software (lead), supervision (lead), validation (lead), visualization (lead), writing – original draft (lead), writing – review & editing (lead).

Funding This research was supported by UK NERC grant GR3/4461 at the University of Leeds.

Data availability All data generated or analysed during this study are included in this published article (and, if present, its supplementary information files).

References

Adams, B.L., Wright, S.I. and Kunze, K. 1993. Orientation imaging: the emergence of a new microscopy. *Metallurgical Transactions*, **A24**, 819–831, https://doi.org/10.1007/BF02656503

Aizu, K. 1970. Possible species of ferromagnetic, ferroelectric, and ferroelastic crystals. *Physical Review B2*, 754–772.

Aizu, K. 1973. Second-order ferroic state shifts. *Journal of the Physical Society of Japan*, **34**, 121–128, https://doi.org/10.1143/JPSJ.34.121

Amouyal, Y., Rabkin, E. and Mishin, Y. 2005. Correlation between grain boundary energy and geometry in Ni-rich NiAl. *Acta Materiallia*, **53**, 3795–3805, https://doi.org/10.1016/j.actamat.2005.04.043

Anderson, T.L., Newnham, R.E., Cross, L.E. and Laughner, J.W. 1976. Laser-induced twinning in quartz. *Physica Status Solidi*, **37**, 235–245, https://doi.org/10.1002/pssa.2210370130

Berka, L. 1982. On stress distribution in a structure of polycrystals. *Journal of Materials Science*, **17**, 1508–1512, https://doi.org/10.1007/BF00752267

Brandon, D.G. 1966. The structure of high-angle grain boundaries. *Acta Metallurgica*, **14**, 1479–1484.

British Geological Survey. 2007. *Assynt, Scotland. Special Sheet, Bedrock, 1:50 000*. Geology Series. British Geological Survey, Keyworth, Nottingham.

Cahn, R.W. 1978. Deformation and recrystallization textures in metals and quartz. *Philosophical Transactions of the Royal Society of London. Series A, Mathematical and Physical Sciences 288, Creep of Engineering*

Materials and of the Earth, 159–176 https://www.jstor.org/stable/74981

Chew, D.M. 2005. 1:2500 Geological Map of South Achill Island and Achill Beg, Western Ireland. *Journal of Maps*, **1**, 18–29, https://doi.org/10.4113/jom.2005.25

Coward, M.P. 1984. The strain and textural history of thin-skinned tectonic zones: examples from the Assynt region of the Moine Thrust Zone, NW Scotland. *Journal of Structural Geology*, **6**, 89–100, https://doi.org/10.1016/0191-8141(84)90087-7

Coward, M.P. 1985. The thrust zones of southern Assynt, Moine Thrust Zone. *Geological Magazine*, **122**, 595–607, https://doi.org/10.1017/S0016756800032015

Cross, I. and Randle, V. 2003. Lowest angle solution v. low-index axis solution for misorientations. *Scripta Materialia*, **48**, 1587–1591, https://doi.org/10.1016/S1359-6462(03)00160-X

Day, A.P. 2008. Spherical EBSD. *Journal of Microscopy*, **230**, 472–486, https://doi.org/10.1111/j.1365-2818.2008.02011.x

Day, A.P. 2009. Spherical Kikuchi maps and other rarities. *In*: Schwartz, A.J., Kumar, M., Adams, B.L. and Field, D.P. (eds) *Electron Backscatter Diffraction in Materials Science*. Springer Nature Switzerland.

De Graef, M. and McHenry, M.E. 2012. Structure of materials: An introduction to crystallography, diffraction and symmetry. Cambridge University Press, Cambridge.

Dingley, D.J. 1987. On line microtexture determination using backscatter Kikuchi diffraction in a scanning electron microscope. *In*: Kallend, J.S. and Gottstein, G. (eds) *Eighth International Conference on Textures of Materials (ICOTOM 8)*. The Metallurgical Society, 189–194.

Dingley, D.J., Meaden, G., Dingley, D.J. and Day, A.P. 2018. A review of EBSD: from rudimentary on line orientation measurements to high resolution elastic strain measurements over the past 30 years. *18th International Conference on Textures of Materials (ICOTOM-18)*, St George, Utah, USA. 375, https://doi.org/10.1088/1757-899X/375/1/012003

Doherty, R.D., Hughes, D.A. *et al*. 1997. Current issues in recrystallization: a review. *Materials Science and Engineering*, **A238**, 219–274, https://doi.org/10.1016/S0921-5093(97)00424-3

Doukhan, J-C. and Trepied, L. 1985. Plastic deformation of quartz single crystals. *Bulletin de Minéralogie*, **108**, 97–123.

Earth Viewer. HHMI BioInteractive, https://www.biointeractive.org/classroom-resources/earthviewer

Eshelby, J.D. 1970. *In*: Kanninen, M.F., Adler, W.F., Rosenfield, A.R. and Jaffee, R.I. (eds) *Inelastic Behaviour of Solids. Science*, **167**, 1761–1762, https://doi.org/10.1126/science.167.3926.1761-a

Gallagher, J.J., Friedman, M., Handin, J. and Sowers, G.M. 1974. Experimental studies relating to microfracture in sandstone. *Tectonophysics*, **21**, 203–247.

Gourdet, S., Jonas, J.J. and Montheillet, F. 1998. Minimum-angle v. low-index axis rotations for representing small- and large-angle grain boundary misorientations in cubic lattices. *Journal of Applied Crystallography*, **31**, 204–211, https://doi.org/10.1107/S0021889897010005

Humphreys, F.J. and Hatherly, M. 2004. *Recrystallization and Related Annealing Phenomena*. Elsevier Ltd, https://doi.org/10.1016/B978-0-08-044164-1.X5000-2

Ishida, Y. and McLean, M. 1973. Burgers vectors of boundary dislocations in ordered grain boundaries of cubic metals. *Philosophical Magazine*, **27**, 1125–1134.

Johnson, M.R.W., Kelley, S.P., Oliver, G.J.H. and Winter, D.A. 1985. Thermal effects and timing of thrusting in the Moine Thrust Zone. *Journal Geological Society of London*, **142**, 863–874, https://doi.org/10.1144/gsjgs.142.5.0863

Kim, C-S., Hu, Y., Rohrer, G.S. and Randle, V. 2005. Five-parameter grain boundary distribution in grain boundary engineered brass. *Scripta Materialia*, **52**, 633–637.

King, A.H. and Shekhar, S. 2006. What does it mean to be special? The significance and application of the Brandon criterion. *Journal of Material Science*, **41**, 7675–7682, https://doi.org/10.1007/s10853-006-0665-8

Klassen-Neklyudova, M.V. 1964. Mechanical twinning of crystals. New York: Consultants Bureau, Springer.

Knipe, R.J. 1990. Microstructural analysis and tectonic evolution in thrust systems: examples from the Assynt region of the Moine Thrust Zone, NW Scotland. *In*: Barber, D.J. and Meredith, P.G. (eds) *Deformation Processes in Minerals, Ceramics and Rocks*. The Mineralogical Society, Special Publications, **1**, 228–261.

Knipe, R.J. and Lloyd, G.E. 1994. Microstructural analysis of faulting in quartzite, Assynt, NW Scotland: implications for fault zone evolution. *Pure and Applied Geophysics*, **143**, 229–254, https://doi.org/10.1007/BF00874330

Langdon, T.G. 2006. Grain boundary sliding revisited: Developments in sliding over four decades. *Journal of Materials Science*, **41**, 597–609.

Liu, W., Icea, G.E., Larsonb, B.C., Yangb, W. and Tischler, J.Z. 2005. Non-destructive three-dimensional characterization of grain boundaries by X-ray crystal microscopy. *Ultramicroscopy*, **103**, 199–204, https://doi.org/10.1016/j.ultramic.2004.11.022

Lloyd, G.E. 1987. Atomic number and crystallographic contrast images with the SEM: a review of backscattered electron techniques. *Mineralogical Magazine*, **51**, 3–19, https://doi.org/10.1180/minmag.1987.051.359.02

Lloyd, G.E. 2000. Grain boundary contact effects during faulting of quartzite: an SEM/EBSD analysis. *Journal of Structural Geology*, **22**, 1675–1693, https://doi.org/10.1016/S0191-8141(00)00069-9

Lloyd, G.E. 2004. Microstructural evolution in a mylonitic quartz simple shear zone: the significant roles of Dauphine twinning and misorientation. *Geological Society, London, Special Publications*, **224**, 39–61, https://doi.org/10.1144/GSL.SP.2004.224.01.04

Lloyd, G.E. and Ferguson, C.C. 1986. A spherical electron-channelling pattern map for use in quartz petrofabric analysis. *Journal of Structural Geology*, **8**, 517–526, https://doi.org/10.1016/0191-8141(86)90002-7

Lloyd, G.E. and Knipe, R.J. 1992. Deformation mechanisms accommodating faulting of quartzite under upper crustal conditions. *Journal of Structural Geology*, **14**, 127–143, https://doi.org/10.1016/0191-8141(92)90052-X

Lloyd, G.E., Farmer, A.B. and Mainprice, D. 1997. Misorientation analysis and the formation and orientation of subgrain and grain boundaries. *Tectonophysics*, **279**, 55–78, https://doi.org/10.1016/S0040-1951(97)00115-7

Lloyd, G.E., Lee, A.L. and Kahl, M. 2021. A practical method to determine the five-parameter orientation of intragranular boundaries in polycrystals. *Tectonophysics*, **814**, 228995, https://doi.org/10.1016/j.tecto.2021.228955

Mainprice, D., Lloyd, G.E. and Casey, M. 1993. Individual orientation measurements in quartz polycrystals – advantages and limitations for texture and petrophysical property determinations. *Journal of Structural Geology*, **15**, 1169–1187, https://doi.org/10.1016/0191-8141(93)90162-4

Mainprice, D., Hielscher, R. and Schaeben, H. 2011. Calculating anisotropic physical properties from texture data using the MTEX open-source package. *Geological Society, London, Special Publications*, **360**, 175–192, https://doi.org/10.1144/SP360.10

Menegon, L., Piazolo, S. and Pennacchioni, G. 2011. The effect of Dauphiné twinning on plastic strain in quartz. *Contributions to Mineralogy and Petrology*, **161**, 635–652, https://doi.org/10.1007/s00410-010-0554-7

Minor, A., Rybacki, E., Sintubin, M., Vogel, S. and Wenk, H.-R. 2018. Tracking mechanical Dauphiné twin evolution with applied stress in axial compression experiments on a low-grade metamorphic quartzite. *Journal of Structural Geology*, **112**, 81–94, https://doi.org/10.1016/j.jsg.2018.04.002

Mørk, M.B.E. and Moen, K. 2007. Compaction microstructures in quartz grains and quartz cement in deeply buried reservoir sandstones using combined petrography and EBSD analysis. *Journal of Structural Geology*, **29**, 1843–1854, https://doi.org/10.1016/j.jsg.2007.08.004

Muto, J., Hirth, G., Heilbronner, R. and Tullis, J. 2011. Plastic anisotropy and fabric evolution in sheared and recrystallized quartz single crystals. *Journal of Geophysical Research*, **116**, B02206, doi:10.1029/2010JB007891.

Newnham, R.E. 1975. Structure-property relations. Berlin: Springer-Verlag. 78–114.

Newnham and Cross. 1974. Symmetry of secondary ferroics. II. *Materials Research Bulletin*, **9**, 1021–1031.

Newnham, R.E., Miller, C.S., Cross, L.E. and Cline, T.W. 1975. Tailored domain patterns in piezoelectric crystals. *Physica Status Solidi*, **32**, 69–78.

Palumbo, G., Aust, K.T., Lehockey, E.M., Erb, U. and Lin, P. 1998. On a more restrictive geometric criterion for 'special' CSL grain boundaries. *Scripta Materiallia*, **38**, 1685–1690.

Paterson, M. S. 1973. Nonhydrostatic thermodynamics and its geologic applications. *Reviews of Geophysics and Space Physics*, **11**, 355–389.

Pennock, G.M., Coleman, M., Drury, M.R. and Randle, V. 2009. Grain boundary plane populations in minerals: the example of wet NaCl after low strain deformation. *Contributions to Mineralogy and Petrology*, **158**, 53–67.

Pumphrey, P.H. 1972. A plane matching theory of high angle grain boundary structure. *Scripta Metallurgica*, **6**, 107–114, https://doi.org/10.1016/0036-9748(72)90260-8

Pumphrey, P.H. 1976. Boundary structure and properties. *In*: Smith, D.A. and Chadwick, G.A. (eds) *Grain Boundary Structure and Properties*. Academic Press, London, 139–200.

Randle, V. 2001. A methodology for grain boundary plane assessment by single section trace analysis. *Scripta Materiallia*, **44**, 2789–2794, https://doi.org/10.1016/S1359-6462(01)00975-7

Randle, V. 2003. *Microtexture Determination and its Application*, 2nd edn. Maney Press, London.

Randle, V. 2004. Application of electron backscatter diffraction to grain boundary characterisation. *International Materials Reviews*, **49**, 1–11, https://doi.org/10.1179/095066004225010514

Randle, V. 2006. 'Five-parameter' analysis of grain boundary networks by electron backscatter diffraction. *Journal of Microscopy*, **222**, 69–75, https://doi.org/10.1111/j.1365-2818.2006.01575.x

Randle, V., Davies, P. and Hulm, B. 1999. Grain-boundary plane reorientation in copper. *Philosophical Magazine*, **A79**, 305–316, https://doi.org/10.1080/01418619908210299

Read, W.T. and Shockley, W. 1950. Dislocation models of crystal grain boundaries. *Physics Review*, **78**, 275–289, https://doi.org/10.1103/PhysRev.78.275

Rohrer, G.S. 2011. Grain boundary energy anisotropy: a review. *Journal of Materials Science*, **46**, 5881–5895, https://doi.org/10.1007/s10853-011-5677-3

Rohrer, G.S. and Randle, V. 2009. Measurement of the five parameter grain boundary distribution from planar sections. *In*: Schwartz, A.J., Kumar, M., Adams, B.L. and Field, D.P. (eds) *Electron Backscatter Diffraction in Materials Science*. Springer.

Sander, B. 1950. *Einführung in die Gefügekunde der Geologischen Körper, Zweiter Teil: die Korngefüge*. Springer, Vienna.

Smith, W. 1815. *A Memoir to the Map and Delineation of the Strata of England and Wales with Part of Scotland*. John Cary, London.

Sutton, A.P. and Balluffi, R.W. 1995. *Interfaces in Crystalline Materials*. Oxford University Press, Oxford.

Sutton, A.P., Banks, E.P. and Warwick, A.R. 2015. The five-dimensional parameter space of grain boundaries. *Proceedings of the Royal Society*, **A471**, 20150442, https://doi.org/10.1098/rspa.2015.0442

Swett, K. 1969. Interpretation of the depositional and diagenetic history of the Cambro-Ordovician succession of Northwest Scotland. *In*: Kay, M. (ed.) *North Atlantic – Geology and Continental Drift*. American Association of Petroleum Geologists, Memoirs, **12**, 630–646.

Szaniawska, L. 2018. Lithological maps visualizing the achievements of geological sciences in the first half of the nineteenth century. *Polish Cartographical Review*, **50**, 87–109, https://doi.org/10.2478/pcr-2018-0006

Thigpen, J.R., Law, R.D., Lloyd, G.E., Brown, S.J. and Cook, B. 2010. Deformation temperatures, vorticity of flow and strain symmetry in the Loch Eriboll mylonites, NW Scotland: implications for kinematic and structural evolution of the northernmost Moine thrust zone. *Geological Society, London, Special Publications*, **335**, 623–662, https://doi.org/10.1144/SP335.26

Thomas, L.A. and Wooster, W.A. 1951. Piezoerescence – the growth of Dauphiné twinning in quartz under stress. *Proceedings of the Royal Society, London*, **A208**, 43–63, https://doi.org/10.1098/rspa.1951.0143

Tullis, J. 1970. Quartz preferred orientation in rocks produced by Dauphiné twinning. *Science*, **168**, 1342–1344, https://doi.org/10.1126/science.168.3937.1342

Tullis, J. and Tullis, T. 1972. Preferred orientation of quartz produced by mechanical Dauphiné twinning: thermodynamics and axial experiments. *In*: Heard, H.C. *et al*. (eds) *Flow and Fracture of Rocks*. Geophysical Monograph Series, Washington, American Geophysical Union, no. 16, 67–82.

Valcke, S.L.A., Pennock, G.M., Drury, M.R. and De Breser, J.H.P. 2006. Electron backscatter diffraction as a tool to quantify subgrains in deformed calcite. *Journal of Microscopy*, **224**, 264–276, https://doi.org/10.1111/j.1365-2818.2006.01698.x

Warrington, D.H. and Boon, M. 1975. Ordered structures in random grain boundaries; some geometrical probabilities. *Acta Metallurgica*, **23**, 599–607, https://doi.org/10.1016/0001-6160(75)90100-5

Watanabe, T. 1983. Observations of plane-matching grain boundaries by electron channelling patterns. *Philosophical Magazine*, **A47**, 141–146, https://doi.org/10.1080/01418618308243114

Watanabe, T., Fujii, H., Oikawa, H. and Arai, K.I. 1989. Grain boundaries in rapidly solidified and annealed Fe–6.5 mass% Si polycrystalline ribbons with high ductility. *Acta Metallurgica*, **37**, 941–952, https://doi.org/10.1016/0001-6160(89)90021-7

Wheeler, J., Prior, D.J., Jiang, Z., Speiss, R. and Trimby, P.W. 2001. The petrological significance of misorientations between grains. *Contributions to Mineralogy and Petrology*, **141**, 109–124, https://doi.org/10.1007/s004100000225

White, S. 1977. Geological significance of recovery and recrystallisation processes in quartz. *Tectonophysics*, **37**, 143–170, https://doi.org/10.1016/0040-1951(77)90093-2

Wolf, D. and Lutsko, J.F. 1989. On the geometrical relationship between tilt and twist grain boundaries. *Zeitschrift für Kristallographie*, **189**, 239–262, https://doi.org/10.1524/zkri.1989.189.3-4.239

Wright, S.I. and Adams, B.J. 1992. Automatic analysis of electron backscatter diffraction patterns. *Metallurgical Transactions: A-Physical Metallurgy and Materials Science*, **23**, 759–767, https://doi.org/10.1007/BF02675553

Zaefferer, S. and Elhami, N. 2014. Theory and application of electron channelling contrast imaging under controlled diffraction conditions. *Acta Materialia*, **75**, 20–50, https://doi.org/10.1016/j.actamat.2014.04.018